PC Analysis of Stochastic Differential Equations driven by Wiener noise[☆]

O.P. Le Maître[a,b,c,*], O.M. Knio[b,c,*]

[a] *LIMSI-CNRS, rue John von Neumann, BP 133, Bt 508, F-91403 Orsay Cedex, France*

[b] *Department of Mechanical Engineering and Materials Science, Duke University, Durham, NC 27708, United States*

[c] *CEMSE Division, King Abdullah University of Science and Technology, Thuwal, Kingdom of Saudi Arabia*

Abstract

A polynomial chaos (PC) analysis with stochastic expansion coefficients is proposed for stochastic differential equations driven by additive or multiplicative Wiener noise. It is shown that for this setting, a Galerkin formalism naturally leads to the definition of a hierarchy of stochastic differential equations governing the evolution of the PC modes. Under the mild assumption that the Wiener and uncertain parameters can be treated as independent random variables, it is also shown that the Galerkin formalism naturally separates parametric uncertainty and stochastic forcing dependences. This also enables us to perform an orthogonal decomposition of the process variance, and consequently identify contributions arising from the uncertainty in parameters, the stochastic forcing, and a coupled term. Insight gained from this decomposition is illustrated in light of implementation to simplified linear and non-linear problems; the case of a stochastic bifurcation is also considered.

Key words: stochastic differential equation, Wiener noise, polynomial chaos, variance analysis

1. Introduction

The simulation of complex systems frequently necessitates the simulation of stochastic differential equations. Well-known examples include chemical kinetics [14, 15, 16, 17, 18, 28, 11], small-scale hydrodynamics [21, 42, 3, 10], as well as large-scale ocean and atmosphere models relying on stochastic parametrizations of unresolved scales [4, 20, 27]. In many cases, one is also faced additional challenges associated with the lack of complete knowledge of model parameters, or generally with uncertain model data. These uncertainties compound the challenges of simulating the stochastic dynamics. Conversely, in the presence of irreducible noise, the problems of quantifying the impact of uncertainties, assessing sensitivities, calibrating parameters and assimilating data, become even more daunting.

A basic challenge in the simulation of stochastic systems involving uncertain parameters concerns the need to quantify the impact of uncertain model parameters on the resulting properties or dynamics. Classically, this has been restricted to analyzing the behavior of low order moments, namely the mean and variance of the solution or of selected observables. Various approaches have been applied for the purpose of mean and variance analysis, typically combining sampling methods to account for stochastic forcing, with either sampling techniques or functional representations to account for uncertain model inputs [36, 37, 31, 32, 29, 30, 1].

In this work, we introduce a new methodology for simulating and analyzing stochastic differential equations in the presence of uncertain inputs. We restrict our attention to the situations in which the forcing is

[☆] This work was supported by the US Department of Energy (DOE), Office of Science, Office of Advanced Scientific Computing Research, under Award Number DE-SC0008789.

[*] Corresponding author

Email addresses: olm@limsi.fr (O.P. Le Maître), omar.knio@duke.edu (O.M. Knio)

continuous, more specifically on stochastic differential equations driven by additive or multiplicative Wiener noise. Under the mild assumption that the Wiener noise and uncertain parameters can be treated as independent random variables, this setting enables us to rely on L_2 theory, defined on an abstract probability space in which an "event" can, in its simplest form, be conceptually associated with a specific realization of both the Wiener process and of the uncertain vector of data inputs. Within this framework, we rely on polynomial chaos (PC) representations [41, 5, 12, 23] to represent uncertain model inputs and their impact on the solution, and show that implementation of a Galerkin formalism naturally leads to the definition of a hierarchy of stochastic differential equations governing the evolution of the PC modes of the overall solution. A key advantage of this approach is that, in addition to providing a complete characterization of the stochastic modes of the solution, it also enables us to perform an *orthogonal* decomposition of the process variance, and consequently identify contributions arising from the uncertainty in parameters, the stochastic forcing, and a coupled term.

Combined, our reliance on an L_2 characterization of the impact of uncertain parameters, our ability to perform an orthogonal decomposition of the variance, and the mild assumptions on the nature of the stochastic forcing distinguish the present construction from relevant recent efforts. In particular, Chen et al. [6] considered the case of on an uncertain structure subjected to random forcing, focusing on situations in which noise can be suitably represented by a finite set of canonical random variables. This enabled them to approach the problem in terms of unified treatment of the uncertain structural properties and the stochastic forcing, specifically using an extended random vector that represents their impact. Within this framework, a sampling based probability density approach is developed to capture the response of the uncertain structure to random excitation. While the approach is shown to be quite effective, its extension to situations involving non-smooth stochastic forcing terms is generally challenging, and the approach does not afford a decomposition of the process variance into individual orthogonal components.

The modelling of stochastic systems using functional representations has also been subject of recent efforts, namely based on PC, dynamically orthogonal (DO) decompositions, as well as hybrid PC-DO approaches [7, 33, 35, 34]. In [7, 33], the methodology exploits the smooth character of the stochastic source terms, which leads to compact modal representations that are evolved by simulating governing equations for the modal coefficients. While the works in [7, 33] do not simultaneously address parametric uncertain and random fluctuations, the framework can naturally accommodate both sources. However, extension of the methodology to situations involving non-smooth stochastic forcing, and to enable a decomposition of the solution variance does not appear to be evident. The recent developments in [35, 34] also rely on DO decomposition, but evolve the DO modes based on deriving governing equations for the mean and covariance of the solution, and using an appropriate closure for the evolution of covariance. This framework allows one to consider consider mild assumptions on structure of the stochastic noise, similar to what we consider in the present work. On the other hand, extension of the methodology to incorporate parametric uncertainties and to isolate contributions of uncertain parameters and random forcing is not obvious.

In order to illustrate the features of the present constructions, we focus on the case of a stochastic ordinary differential equation, with uncertain inputs parametrized using a low-dimensional germ (number of independent inputs). Section 2 briefly outlines the setting adopted for the governing system, and introduces basic definitions and notations. Section 3 then introduces the framework for parametric uncertainty, and the functional representations used to express the dependence of the solution on these parameters, as well as the Galerkin formalism used to describe the stochastic dynamics governing the coefficients in the PC representation. In section 4, we outline how this machinery can be implemented to construct an orthogonal decomposition of the variance of the solution. Insight gained from this decomposition is illustrated in Section 5, namely in light of implementations to simplified linear problems, and in Section 6 using simulations of a non-linear problem involving an unstable fixed point. Major conclusions are summarized in Section 7.

2. Stochastic Ordinary Differential Equation (SODE) with Parametric Uncertainty

Consider the generic stochastic ordinary differential equation (SODE),

$$dX(t,\omega) = C(X(t,\omega))dt + D(X(t,\omega))dW(t,\omega), \tag{1}$$

where $X : (t, \Omega) \in T \times \Omega \mapsto \mathbb{R}$ is a real-valued stochastic process, $T \doteq [0, T_f]$ with $T_f > 0$, and $W(t, \omega)$ is the Wiener process. The functions $C : \mathbb{R} \mapsto \mathbb{R}$ and $D : \mathbb{R} \mapsto \mathbb{R}_+$ are are the drift and diffusion coefficient respectively. Equation (1) is complemented by an initial condition, say $X(t = 0, \omega) = X^0(\omega)$. The developments below can be readily extended to the case of non-autonomous SODEs.

2.1. Parametric uncertainty

In most settings, one focuses on the simplified situation where the stochasticity of the system is solely induced by the Wiener process. In the present work, we consider the generalized situation where the initial condition, the drift and the diffusion coefficient also depend on an uncertain parameter vector, U, whose coordinates have known probability law. The continuous SODE is then recast as:

$$dX(t, \omega) = C(X(t, \omega), U(\omega))dt + D(X(t, \omega), U(\omega))dW(t, \omega), \quad X(t = 0, \omega) = X^0(U(\omega)). \tag{2}$$

The fundamental assumption supporting the subsequent developments is that the random parameters $U(\omega)$ of the SODE and the Wiener process $W(t, \omega)$ are *independent*. As a result, the stochastic process $X(t, \omega)$ can be seen as a functional of two independent random quantities, the Wiener process $W(t, \omega)$ and the model parameters $U(\omega)$. Our objective is then to compute $X(t, \omega)$, and to express the solution in a format that enables us to perform a sensitivity analysis of the solution to different sources of uncertainty.

2.2. Discrete form

Classical SODEs are solved by simulation techniques, such as Monte-Carlo methods. To this end, consider a time mesh $t_i = i\Delta t$, $i = 0, 1, 2, \ldots, N_t$ and $\Delta t \equiv T_f/N_t$. On this mesh, the stochastic process can be discretized as $X^i(\omega) = X(t_i, \omega)$. For simplicity of the exposition, we rely on the simplest time integration scheme to solve (2). Specifically, using the Euler forward scheme, the discrete solution, X^i is given by:

$$X^{i+1}(\omega) = X^i(\omega) + C(X^i(\omega), U(\omega))\Delta t + D(X^i(\omega), U(\omega))\Delta W^i(\omega) \quad i = 0, 1, \ldots, N_t - 1. \tag{3}$$

where $\Delta W^i(\omega)$, $i = 1, 2, \ldots$ are independent identically distributed (iid) Gaussian random variables with zero mean and variance Δt.

Sampling based or Monte-Carlo (MC) methods can be used to simulate realizations of X^i, from which one can estimate various quantities of interest, moments, correlations, expectation of some functionals of X, etc... In its simplest form, the MC method consists in generating M pseudo-random sequences of the Wiener increments, $\{\Delta W^i_j, i = 0, \ldots, N_t - 1, j = 1, \ldots, M\}$, together with *independent* sampling of U, $\{U_j, j = 1, \ldots, M\}$, where j refers to the sequence sample index. For each j, one then solves

$$X^{i+1}_j = X^i_j + C(X^i_j, U_j)\Delta t + D(X^i_j, U_j)\Delta W^i_j, \quad i = 0, 1, \ldots, N_t - 1, \tag{4}$$

to obtain a set of M trajectories $\{X_j, j = 1, \ldots, M\}$ of $X(t, \omega)$. Finally, given a functional g, one can estimate the expectation of $g(X)$ through

$$\mathbb{E}\{g(X)\} \approx \frac{1}{M}\sum_{j=1}^{M} g(X_j). \tag{5}$$

For the purpose of uncertainty analysis, and in order to separate the effects of the Wiener process and of the parametric uncertainty, it is often necessary to proceed from MC estimates of a *conditional value* of X. For instance, one may be interested in computing the variance of the expectation of X conditioned on U, that is $\mathbb{V}\{\mathbb{E}\{X \mid U\}\}$. Using the independence of U and W, the MC estimate requires a nested approach where one first solves, for a fixed realization U_k of the parameters, the M resulting trajectories according to

$$X^i_{j,k} = X^{i-1}_{j,k} + C(X^{i-1}_j, U_k)\Delta t + D(X^{i-1}_{j,k}, U_k)\Delta W^i_j, \quad i = 1, 2, \ldots, N_t, \tag{6}$$

and then using the predictions $X_{j,k}$ to estimate the conditional expectation $\mathbb{E}\{X \mid U_k\} \approx \frac{1}{M}\sum_{j=1}^{M} X_{j,k} = \mu_k$. Repeating this process for each U_k, the variance $\mathbb{V}\{\mathbb{E}\{X \mid U\}\}$ can be estimated through

$$\mathbb{V}\{\mathbb{E}\{X \mid U\}\} \approx \frac{1}{M-1}\sum_{k=1}^{M}\mu_k^2 - \left(\frac{1}{M}\sum_{k=1}^{M}\mu_k\right)^2. \tag{7}$$

We observe that this procedure may not necessarily use the same sample set size for W and U, and that different sample sets of the Wiener processes can be used for different parameter samples U_k (in particular for parallelization and error balancing). The main observation is that, regardless of the details of the MC sampling method selected, distinguishing between the effects of parameter uncertainty and intrinsic noise (Wiener) requires successive averaging, and consequently information loss. This has motivated the approach proposed below where such conditional sampling is avoided.

3. Hybrid Galerkin-MC Method for SODEs with Parametric Uncertainty

In this section, we propose an alternative approach to account for parametric uncertainty in SODEs. We first introduce Wiener-like (functional) expansions for random quantities depending on uncertain parameters only. We then introduce an extension of such functional expansions, namely to represent the solution of SODEs also involving irreducible noise.

3.1. Functional expansion

We shall assume in the following that the uncertainty vector, U, is parameterized by a uncertainty germ of N real-valued independent random variables $\boldsymbol{\xi} = \{\xi_1, \ldots, \xi_{\mathrm{N}}\}$. In other words, $U(\omega) = U(\boldsymbol{\xi}(\omega))$. We denote, respectively, by $\Xi_i \in \mathbb{R}$ and p_i the range and density of ξ_i, $i = 1, \ldots, \mathrm{N}$, and by $\Xi \in \mathbb{R}^{\mathrm{N}}$ the range and $p_{\boldsymbol{\xi}}$ the joint-density of $\boldsymbol{\xi}$. Elements of $\boldsymbol{\xi}$ being independent, Ξ and $p_{\boldsymbol{\xi}}$ have product structures

$$\Xi = \prod_{i=1}^{\mathrm{N}}\Xi_i, \quad p_{\boldsymbol{\xi}}(x_1, \ldots, x_{\mathrm{N}}) = \prod_{i=1}^{\mathrm{N}} p_i(x_i), \quad \int_{\Xi} p_{\boldsymbol{\xi}}(\boldsymbol{x})d\boldsymbol{x} = \prod_{i=1}^{\mathrm{N}}\left(\int_{\Xi_i} p_i(x_i)dx_i\right) = 1.$$

Let $L_2(\Xi, p_{\boldsymbol{\xi}})$, or simply L_2 when no confusion is possible, be the space of second-order functionals in $\boldsymbol{\xi}$, equipped with the inner product and associated norm denoted $\langle\cdot,\cdot\rangle$ and $\|\cdot\|_{L_2}$ respectively:

$$\forall U, V \in L_2(\Xi, p_{\boldsymbol{\xi}}), \quad \langle U, V\rangle \doteq \int_{\Xi} U(\boldsymbol{x})V(\boldsymbol{x})p_{\boldsymbol{\xi}}(\boldsymbol{x})d\boldsymbol{x}; \quad \|U\|_{L_2} \doteq \langle U, U\rangle^{1/2} < \infty \Leftrightarrow U \in L_2(\Xi, p_{\boldsymbol{\xi}}).$$

Introducing an orthonormal basis $\{\Psi_k(\boldsymbol{\xi}); k \in \mathbb{N}\}$ for $L_2(\Xi, p_{\boldsymbol{\xi}})$ any second-order randon variable $U(\boldsymbol{\xi})$ can be expanded as

$$L_2(\Xi, p_{\boldsymbol{\xi}}) \ni U(\boldsymbol{\xi}) = \sum_{k\in\mathbb{N}} [U_k]\,\Psi_k(\boldsymbol{\xi}).$$

The coefficients $[U_k]$ are also referred to as modes of U. Classical choices for the basis functionals are the set of multivariate polynomials or multiwavelets in $\boldsymbol{\xi}$ (see section 5). The orthonormality of the basis is expressed as:

$$\langle\Psi_k, \Psi_l\rangle = \int_{\Xi}\Psi_k(\boldsymbol{x})\Psi_l(\boldsymbol{x})p_{\boldsymbol{\xi}}(\boldsymbol{x})d\boldsymbol{x} = \delta_{kl} = \begin{cases} 1 & k = l, \\ 0 & \text{otherwise.}\end{cases}$$

Returning to our problem of computing $X(t, \omega)$ governed by Eq. (2), we first observe that X depends on the uncertain parameters $U(\boldsymbol{\xi}(\omega))$ and on the Wiener process $W(t, \omega)$, which as previously noted are assumed independent. If $X \in L_2(\Xi, p_{\boldsymbol{\xi}})$ for $t > 0$ and for almost any trajectory of $W(t)$, we are lead to consider the separated representation,

$$X(t, \omega) = \sum_{k\in\mathbb{N}} [X_k]\,(t, \omega)\Psi_k(\boldsymbol{\xi}(\omega)), \tag{8}$$

where the *random processes* $[X_k]$, $k \in \mathbb{N}$, are independent of $\boldsymbol{\xi}$, but are functions of $W(t, \omega)$.

3.2. Hybrid Galerkin sampling method

We now need to derive equations that enable us to determine the stochastic processes $[X_k](t,\omega)$. We follow the stochastic Galerkin approach proposed in [12] for this purpose. Specifically, we introduce the expansion (8) into Eq. (2) and project the resulting equation on the stochastic basis, taking the inner product in $L_2(\Xi, p_{\boldsymbol{\xi}})$ with each of the functional Ψ_k. Using the orthonormality of the basis functionals, we obtain for all $k \in \mathbb{N}$

$$\begin{aligned} d[X_k](t,\omega) = &\left\langle C\left(\sum_{l\in\mathbb{N}}[X_l](t,\omega)\Psi_l(\boldsymbol{\xi}), U(\boldsymbol{\xi})\right)dt, \Psi_k(\boldsymbol{\xi})\right\rangle \\ &+\left\langle D\left(\sum_{l\in\mathbb{N}}[X_l](t,\omega)\Psi_l(\boldsymbol{\xi}), U(\boldsymbol{\xi})\right)dW(t,\omega), \Psi_k(\boldsymbol{\xi})\right\rangle. \end{aligned}$$

Using the fact that $W(t,\omega)$ is independent of $\boldsymbol{\xi}$, the above equation can be recast as

$$d[X_k] = \left\langle C\left(\sum_{l\in\mathbb{N}}[X_l]\Psi_l, U\right), \Psi_k\right\rangle dt + \left\langle D\left(\sum_{l\in\mathbb{N}}[X_l]\Psi_l, U\right), \Psi_k\right\rangle dW, \quad \forall k \in \mathbb{N}.$$

For computational purposes, this infinite sequence of coupled problems must be truncated. Assuming that the expansion of X is truncated to its first $P+1$ terms, we get the following system of $P+1$ coupled stochastic differential equations:

$$d[X_k] = [C_k]([X_0],\dots,[X_P])dt + [D_k]([X_0],\dots,[X_P])dW, \quad k = 0,\dots,P \tag{9}$$

where we have denoted

$$[C_k]([X_0],\dots,[X_P]) \doteq \left\langle C\left(\sum_{l=0}^{P}[X_l]\Psi_l, U\right), \Psi_k\right\rangle, \tag{10}$$

$$[D_k]([X_0],\dots,[X_P]) \doteq \left\langle D\left(\sum_{l=0}^{P}[X_l]\Psi_l, U\right), \Psi_k\right\rangle. \tag{11}$$

This system of SODEs has to be complemented by initial conditions which are simply obtained by projecting the initial data on the stochastic basis

$$[X_k](t=0) = \left\langle X^0, \Psi_k\right\rangle. \tag{12}$$

Aggregating the modes into vectors, we finally have to solve

$$d\boldsymbol{X} = \boldsymbol{C}(\boldsymbol{X})dt + \boldsymbol{D}(\boldsymbol{X})dW, \quad \boldsymbol{X}(t=0) = \boldsymbol{X}^0, \tag{13}$$

where $\boldsymbol{X}^0$ is given in component form by Eq.(12).

Again, the system of SODEs can be solved using standard Monte-Carlo simulation, introducing a time scheme and generating trajectories for the Wiener-process. We emphasize that the modes $[X_k]$ are all driven by a *unique* Wiener process. Following the notations of section 2.2, the time-discretized system for the Euler method becomes

$$\boldsymbol{X}^{i+1}(\omega) = \boldsymbol{X}^i(\omega) + \boldsymbol{C}(\boldsymbol{X}^i)\Delta t + \boldsymbol{D}(\boldsymbol{X}^i)\Delta W^i(\omega), \quad i = 0,1,\dots \tag{14}$$

For the j-th sample trajectory of the discretized Wiener process increments, $\{\Delta W_j^i = W^{i+1}(\omega_j) - W^i(\omega_j), i = 0,1,\dots\}$, we obtain the following discrete approximation

$$X_j^i(\boldsymbol{\xi}) \approx \sum_{k=0}^{P}[X_k]_j^i\Psi_k(\boldsymbol{\xi}), \tag{15}$$

where the vector of expansion coefficients $\boldsymbol{X}_j^i = ([X_0]_j^i, \cdots, [X_P]_j^i)^T$ solves Eq. (14). We emphasize that $X_j^i(\boldsymbol{\xi})$ in Eq. (15) is still a random quantity, being dependent on the model parameters.

The main computational difficulty in solving the system comes from the projection of the drift and diffusion coefficients appearing in Eqs. (10)-(11). To this end, one can rely for instance on pseudo-spectral projection methods (see discussions in [9, 23]). This point will be further discussed in the result sections on the basis of the examples provided.

4. Variance Decomposition of noise / parameter contributions

In this section, we provide expressions to retrieve the second-order properties of the uncertain stochastic process from its PC expansion. Having determined the conditional expectations and variances, we introduce the Sobol-Hoeffding (SH) decomposition of the process, to separate X into orthogonal functionals in the parameters, noise and coupled contribution. The SH decomposition is further exploited to derive the expression of the sensitivity indices, allowing for a fine analysis of the impact of the distinct sources of randomness on the process. Finally, we briefly discus computational aspects for Monte-Carlo estimation of the variance decomposition. In the remainder of the section, we drop the time dependence to simplify the notation.

4.1. Mean and Total Variance

The mean of the process, $\bar{X} = \mathbb{E}\{X\}$, is immediately obtained from the PC expansion of X as follows

$$\mathbb{E}\{X\} \approx \mathbb{E}\left\{\sum_{k=0}^{P} [X_k]\,\Psi_k\right\} = \sum_{k=0}^{P} \mathbb{E}\{[X_k]\}\,\mathbb{E}\{\Psi_k\} = \mathbb{E}\{[X_0]\}\,. \tag{16}$$

Here, we used the convention $\Psi_0 = 1$ and exploited the independence of the random PC coefficients $[X_k](\omega)$ (functions of W only) and basis random functionals $\Psi_k(\boldsymbol{\xi}(\omega))$. In other words, the mean of the process is equal to the average value of the first component of the vector-valued random process $\boldsymbol{X}$. Similarly the (total) variance of the process, $\mathbb{V}\{X\}$, is given by

$$\begin{aligned}
\mathbb{V}\{X\} &= \mathbb{E}\left\{(X - \mathbb{E}\{X\})^2\right\} \approx \mathbb{E}\left\{\left(\sum_{k=0}^{P} [X_k]\,\Psi_k - \mathbb{E}\{[X0]\}\,\Psi_0\right)^2\right\} \\
&= \mathbb{E}\left\{([X_0] - \mathbb{E}\{[X_0]\})^2 - 2\,([X_0] - \mathbb{E}\{[X_0]\})\sum_{k=1}^{P} [X_k]\,\Psi_k + \left(\sum_{k=1}^{P} [X_k]\,\Psi_k\right)^2\right\} \\
&= \mathbb{V}\{[X_0]\} + \sum_{k=1}^{P} \mathbb{E}\left\{[X_k]^2\right\}.
\end{aligned} \tag{17}$$

The above expression shows that the total variance of the process is given by the sum of the variance of the first PC coefficient $[X_0](\omega)$ and the second moments of the higher-order ($P > 0$) PC coefficients.

4.2. Conditional expectations and variances

One advantage of the PC expansion of the uncertain stochastic process is that it enables us to readily determine of the conditional expectations and variances. For instance, the conditional expectation X given $\boldsymbol{\xi} = \boldsymbol{\eta}$ is simply expressed as:

$$\mathbb{E}\{X \mid \boldsymbol{\xi} = \boldsymbol{\eta}\} \approx \mathbb{E}\left\{\sum_{k=0}^{P} [X_k]\,\Psi_k \,\middle|\, \boldsymbol{\xi} = \boldsymbol{\eta}\right\} = \sum_{k=0}^{P} \mathbb{E}\{[X_k]\}\,\mathbb{E}\{\Psi_k \mid \boldsymbol{\xi} = \boldsymbol{\eta}\} = \sum_{k=0}^{P} \mathbb{E}\{[X_k]\}\,\Psi_k(\boldsymbol{\eta}). \tag{18}$$

Additionally, the dependence with respect to the uncertain parameters of the W-average of the process, denoted $\mu_X(\boldsymbol{\xi})$, is simply retrieved from the PC expansion by averaging the coefficients:

$$\mu_X(\boldsymbol{\xi}) = \mathbb{E}\left\{ X \mid \boldsymbol{\xi} \right\} = \sum_{k=0}^{P} \mathbb{E}\left\{ [X_k] \right\} \Psi_k(\boldsymbol{\xi}). \tag{19}$$

Further, the conditional variance of X given that $\boldsymbol{\xi} = \boldsymbol{\eta}$ can be expressed as:

$$\begin{aligned}\mathbb{V}\left\{ X \mid \boldsymbol{\xi} = \boldsymbol{\eta} \right\} &= \mathbb{E}\left\{ \left(X - \mathbb{E}\left\{ X | \boldsymbol{\xi} = \boldsymbol{\eta} \right\} \right)^2 \,\middle|\, \boldsymbol{\xi} = \boldsymbol{\eta} \right\} \approx \mathbb{E}\left\{ \left(\sum_{k=0}^{P} [X_k]\, \Psi_k - \sum_{k=0}^{P} \mathbb{E}\left\{ [X_k] \right\} \Psi_k(\boldsymbol{\eta}) \right)^2 \,\middle|\, \boldsymbol{\xi} = \boldsymbol{\eta} \right\} \\ &= \sum_{k,k'=0}^{P} \left[\mathbb{E}\left\{ [X_k]\, [X_{k'}] \right\} - \mathbb{E}\left\{ [X_k] \right\} \mathbb{E}\left\{ [X_{k'}] \right\} \right] \Psi_k(\boldsymbol{\eta}) \Psi_{k'}(\boldsymbol{\eta}) = \sum_{k,k'=0}^{P} \left[\mathbb{C}_{\boldsymbol{X},\boldsymbol{X}} \right]_{k,k'} \Psi_k(\boldsymbol{\eta}) \Psi_{k'}(\boldsymbol{\eta}),\end{aligned}$$

where we have denoted $[\mathbb{C}_{\boldsymbol{X},\boldsymbol{X}}]$ the covariance matrix of the random vector $\boldsymbol{X}(\omega)$. From this expression, the PC expansion of the W-variance of X as a function $\boldsymbol{\xi}$ can be obtained:

$$\Sigma^2_X(\boldsymbol{\xi}) \approx \sum_{k=0}^{P} \left[\Sigma^2_{X,k} \right] \Psi_k(\boldsymbol{\xi}), \quad \left[\Sigma^2_{X,k} \right] = \sum_{m,n=0}^{P} \left[\mathbb{C}_{\boldsymbol{X},\boldsymbol{X}} \right]_{m,n} \left\langle \Psi_m \Psi_n, \Psi_k \right\rangle. \tag{20}$$

Conversely, the expectation of X conditioned on $W = W(\omega)$ is

$$\begin{aligned}\mathbb{E}\left\{ X \mid W = W(\omega) \right\} &\approx \mathbb{E}\left\{ \sum_{k=0}^{P} [X_k]\, \Psi_k \,\middle|\, W = W(\omega) \right\} \\ &= \sum_{k=0}^{P} \mathbb{E}\left\{ [X_k] \mid W = W(\omega) \right\} \mathbb{E}\left\{ \Psi_k \right\} = [X_0](\omega).\end{aligned} \tag{21}$$

In other words, the parameter-average of X given a realization $W(\omega)$ of the noise is equal to the corresponding realization of the coefficient $[X_0](\omega)$. Similarly, the conditional variance $\mathbb{V}\left\{ X \mid W = W(\omega) \right\}$ can be expressed according to:

$$\begin{aligned}\mathbb{V}\left\{ X \mid W = W(\omega) \right\} &= \mathbb{E}\left\{ \left(X - \mathbb{E}\left\{ X \mid W = W(\omega) \right\} \right)^2 \,\middle|\, W = W(\omega) \right\} \\ &\approx \mathbb{E}\left\{ \left(\sum_{k=0}^{P} [X_k]\, \Psi_k - [X_0](\omega) \right)^2 \,\middle|\, W = W(\omega) \right\} = \sum_{k=1}^{P} [X_k]^2 (\omega).\end{aligned} \tag{22}$$

Therefore, the variance in X due to the parameter given that $W = W(\omega)$ is obtained by the corresponding sum of the squares of the PC coefficients, but the first one.

4.3. Sobol–Hoeffding decomposition

At this point, we have derived from the PC expansion of X expressions for expectations and variances conditioned on W and $\boldsymbol{\xi}$, respectively. We now make use of these expressions to perform the SH decomposition of X [38]. Our objective, based on the fact that X can be seen as a second-order random functional depending on two independent sources of randomness, the noise W and the parameters $\boldsymbol{\xi}$, is to decompose X into

$$X = \bar{X} + X_{\text{par}}(\boldsymbol{\xi}) + X_{\text{noise}}(W) + X_{\text{mix}}(\boldsymbol{\xi}, W), \tag{23}$$

where $\bar{X}$ is the global mean of X, X_{par} is function of $\boldsymbol{\xi}$ (parameters) *only*, X_{noise} is function of W (noise) *only* and X_{mix} depends on *both* $\boldsymbol{\xi}$ and W. Requiring the orthogonality of the decomposition makes it unique, and the functionals are then given by the conditional expectations as follows [38]:

$$X_{\text{par}}(\boldsymbol{\xi}) = \mathbb{E}\left\{ X \mid \boldsymbol{\xi} \right\} - \bar{X}, \tag{24}$$

$$X_{\text{noise}}(W) = \mathbb{E}\left\{ X \mid W \right\} - \bar{X}, \tag{25}$$

$$X_{\text{mix}}(\boldsymbol{\xi}, W) = X + \bar{X} - \mathbb{E}\left\{ X \mid \boldsymbol{\xi} \right\} - \mathbb{E}\left\{ X \mid W \right\}. \tag{26}$$

The orthogonal character of the decomposition can be easily verified observing that $\mathbb{E}\{\mathbb{E}\{X \mid W\}\} = \mathbb{E}\{\mathbb{E}\{X \mid \boldsymbol{\xi}\}\} = \bar{X}$. Using the previous expressions for the conditional expectations in terms of the PC coefficients of X, we obtain:

$$X_{\text{par}}(\boldsymbol{\xi}) = \sum_{k=1}^{P} \mathbb{E}\{[X_k]\}\, \Psi_k(\boldsymbol{\xi}), \tag{27}$$

$$X_{\text{noise}}(W) = [X_0] - \mathbb{E}\{[X_0]\}, \tag{28}$$

$$X_{\text{mix}}(\boldsymbol{\xi}, W) = \sum_{k=1}^{P} \left([X_k] - \mathbb{E}\{[X_k]\}\right) \Psi_k(\boldsymbol{\xi}), \tag{29}$$

providing explicit expressions for the SH decomposition of X in terms of the PC coefficients.

4.4. Sensitivity Analysis

The orthogonality of the SH decomposition (23) leads to a natural decomposition of variance of X into partial variances:

$$\mathbb{V}\{X\} = V_{\text{par}} + V_{\text{noise}} + V_{\text{mix}}, \quad V_\bullet \doteq \mathbb{V}\{X_\bullet\} \text{ for } \bullet = \text{par}, \text{noise}, \text{mix}. \tag{30}$$

The expression of these partial variances, in terms of the stochastic vector $\boldsymbol{X}$ is immediate:

$$V_{\text{par}} = \sum_{k=1}^{P} \mathbb{E}\{[X_k]\}^2, \quad V_{\text{noise}} = \mathbb{V}\{[X_0]\}, \quad V_{\text{mix}} = \sum_{k=1}^{P} \mathbb{V}\{[X_k]\}. \tag{31}$$

These partial variances can be normalized by the total variance $\mathbb{V}\{X\}$ to construct the so-called sensitivity indices used for global sensitivity analysis of X. Specifically, the two first-order sensitivity indices $\mathtt{S}_{\text{par}}$ and $\mathtt{S}_{\text{noise}}$, given by

$$\mathtt{S}_{\text{par}} \doteq \frac{V_{\text{par}}}{\mathbb{V}\{X\}}, \quad \mathtt{S}_{\text{noise}} \doteq \frac{V_{\text{noise}}}{\mathbb{V}\{X\}},$$

respectively measure the fraction of the variance in X that arises *solely* to the two independent sources of variability: the uncertain paramaters and the noise. The second order index $\mathtt{S}_{\text{par,noise}} = V_{\text{mix}}/\mathbb{V}\{X\}$ measures the fraction of the variance caused by the interaction effects between the noise and the parametric uncertainty. Often, global sensitivity analysis (SA) is based on the first order (defined above) and total sensitivity indices, namely

$$\mathtt{T}_{\text{par}} = \frac{V_{\text{par}} + V_{\text{mix}}}{\mathbb{V}\{X\}} \geq \mathtt{S}_{\text{par}}, \quad \mathtt{T}_{\text{noise}} = \frac{V_{\text{noise}} + V_{\text{mix}}}{\mathbb{V}\{X\}} \geq \mathtt{S}_{\text{noise}}.$$

The interpretation of the sensitivity indices is as follows. Whenever $\mathtt{T}_{\text{par}}$ (resp. $\mathtt{T}_{\text{noise}}$) is small, the parametric uncertainty (resp. noise) is deemed to have a negligible impact on the variability of X. When $\mathtt{T}_{\text{par}}/\mathtt{S}_{\text{par}} \geq 1$ (resp. $\mathtt{T}_{\text{noise}}/\mathtt{S}_{\text{noise}} \geq 1$) is close to 1, the effect of the parametric (resp. noise) is said to be essentially additive (exactly additive when equal to 1). In fact, the model is said purely additive when $\mathtt{S}_{\text{par}} + \mathtt{S}_{\text{noise}} = 1$. We observe that the interaction of the parameters and noise is here entirely characterized by the second-order index $\mathtt{S}_{\text{par,noise}}$. When $\mathtt{S}_{\text{par,noise}} = 0$, the noise and parametric uncertainty have additive effects on the model.

Also, in many situations the parametric uncertainty affects distinct and independent components of the model, for instance independent uncertainty in the drift function C on the one hand, and the diffusion coefficient on the other hand. In such a case, one may want to perform a finer sensitivity analysis to compare the impact of different uncertainty sources (and noise). The proposed decomposition above can be extended to perform this type of analysis. The procedure is outlined below.

Recall that the uncertainty in the model is parametrized using a set of N independent r.v., $\boldsymbol{\xi} = \{\xi_1, \cdots, \xi_{\text{N}}\}$. Denoting $\mathcal{N} = \{1, \cdots, \text{N}\}$ the set of uncertain dimensions, we assume that $\mathcal{N}$ can be partitioned into a set $\mathcal{D}$ of $d \leq \text{N}$ distinct sets $\mathcal{D}_i$, referring to independent sources of uncertainties:

$$\mathcal{D} = \{\mathcal{D}_1, \cdots, \mathcal{D}_d\}, \quad \bigcup_{i=1}^{d} \mathcal{D}_i = \mathcal{N}, \quad \mathcal{D}_i \cap \mathcal{D}_{j \neq i} = \emptyset.$$

Then for $\mathtt{u} \subseteq \mathcal{D}$, we denote its complement $\mathtt{u}_\sim \doteq \mathcal{D} \setminus \mathtt{u}$ and $\boldsymbol{\xi}_\mathtt{u} = \{\xi_{\mathtt{u}_1}, \cdots, \xi_{\mathtt{u}_{|\mathtt{u}|}}\}$, where in this context $|\cdot|$ is the cardinality of the set. For instance, $\boldsymbol{\xi}$ can be separated into two independent subsets $\boldsymbol{\xi} = \{\boldsymbol{\xi}_\mathtt{C}, \boldsymbol{\xi}_\mathtt{D}\}$ related to the uncertainty in the drift and diffusion respectively, so $\mathcal{D} = \{\mathtt{C}, \mathtt{D}\}$ with cardinality 2, and $\mathtt{u}$ can be $\emptyset$, $\mathtt{C}$, $\mathtt{D}$ and $\mathtt{C} \cup \mathtt{D}$. The SH decomposition over $\mathcal{D}$ of a functional $F \in L_2(\Xi, p_{\boldsymbol{\xi}})$ can be expressed as $\sum_{\mathtt{u} \subseteq \mathcal{D}} F_\mathtt{u}(\boldsymbol{\xi}_\mathtt{u})$, where the summation involves $2^{|\mathcal{D}|}$ elements. The elements are defined recursively from the conditional expectations as follows:

$$F_\mathtt{u}(\boldsymbol{\xi}_\mathtt{u}) = \mathbb{E}\{F \mid \boldsymbol{\xi}_\mathtt{u}\} - \sum_{\mathtt{v} \subsetneq \mathtt{u}} F_\mathtt{v}(\boldsymbol{\xi}_\mathtt{v}).$$

Returning to our problem, we already have the decomposition of X into parametric, noise and mixed contribution. To further separate contributions of subsets of parameters, say $\mathtt{C}$ and $\mathtt{D}$, we just have to deal with X_{par} and X_{mix}, X_{noise} being independent of $\boldsymbol{\xi}$. We then have to introduce the SH decompositions over $\mathcal{D}$ of X_{par} and X_{mix},

$$X_{\text{par}}(\boldsymbol{\xi}) = \sum_{\substack{\mathtt{u} \subseteq \mathcal{D} \\ \mathtt{u} \neq \emptyset}} X^{\text{par}}_\mathtt{u}(\boldsymbol{\xi}_\mathtt{u}), \quad X_{\text{mix}}(\boldsymbol{\xi}, W) = \sum_{\substack{\mathtt{u} \subseteq \mathcal{D} \\ \mathtt{u} \neq \emptyset}} X^{\text{mix}}_{\mathtt{u},W}(\boldsymbol{\xi}_\mathtt{u}, W), \tag{32}$$

to obtain the generalized SH decomposition of X, over $\mathcal{D}$:

$$X = \bar{X} + \sum_{\substack{\mathtt{u} \subseteq \mathcal{D} \\ \mathtt{u} \neq \emptyset}} X^{\text{par}}_\mathtt{u}(\boldsymbol{\xi}_\mathtt{u}) + X_{\text{noise}}(W) + \sum_{\substack{\mathtt{u} \subseteq \mathcal{D} \\ \mathtt{u} \neq \emptyset}} X^{\text{mix}}_{\mathtt{u},W}(\boldsymbol{\xi}_\mathtt{u}, W).$$

The extended definition of the first order and total sensitivity indices, retaining the separation of parametric and noise contribution for convenience, becomes

$$\begin{aligned} \mathtt{S}_\mathtt{u} = \frac{\mathbb{V}\{X^{\text{par}}_\mathtt{u}\}}{\mathbb{V}\{X\}}, \quad \mathtt{T}_\mathtt{u} = \mathtt{T}^{\text{par}}_\mathtt{u} + \mathtt{T}^{\text{mix}}_\mathtt{u}, \quad \mathtt{T}^{\text{par}}_\mathtt{u} = \sum_{\substack{\mathtt{v} \subseteq \mathcal{D} \\ \mathtt{u} \cap \mathtt{v}}} \frac{\mathbb{V}\{X^{\text{par}}_\mathtt{v}\}}{\mathbb{V}\{X\}}, \quad \mathtt{T}^{\text{mix}}_\mathtt{u} = \sum_{\substack{\mathtt{v} \subseteq \mathcal{D} \\ \mathtt{u} \cap \mathtt{v}}} \frac{\mathbb{V}\{X^{\text{mix}}_{\mathtt{v},W}\}}{\mathbb{V}\{X\}} \\ \mathtt{T}_{\text{noise}} = \mathtt{T}^{\text{noise}}_{\text{noise}} + \mathtt{T}^{\text{mix}}_{\text{noise}}, \quad \mathtt{T}^{\text{noise}}_{\text{noise}} = \frac{\mathbb{V}\{X_{\text{noise}}\}}{\mathbb{V}\{X\}}, \quad \mathtt{T}^{\text{mix}}_{\text{noise}} = \sum_{\substack{\mathtt{u} \subseteq \mathcal{D} \\ \mathtt{u} \neq \emptyset}} \frac{\mathbb{V}\{X^{\text{mix}}_{\mathtt{u},W}\}}{\mathbb{V}\{X\}}. \end{aligned} \tag{33}$$

Observe that $\mathtt{T}_{\text{noise}}$ takes the same value as before, but its expression with summation over elements $\mathtt{u}$ provides an effective means to analyze the impact of different uncertain parameters on the mixed term contribution.

It remains to make explicit the expressions of the partial variances appearing in the definition of the first order and total sensitivity indices. This turns out to be easier than expected if we consider the expressions of the functionals X_{par} and X_{mix} provided in (27) and (29). Since these functionals are expressed as PC expansions in $\boldsymbol{\xi}$, with coefficients in terms of the components of $\boldsymbol{X}$, their decompositions in (32) only amounts to the decomposition of the basis functional $\Psi_k(\boldsymbol{\xi})$. In the case of PC expansions with basis resulting from the tensorization of orthogonal families of univariate polynomials, the SH decomposition of Ψ_k over $\mathcal{D}$ is explicit [8], allowing for the explicit decomposition of a PC expansion. Specifically, we have

$$F(\boldsymbol{\xi}) = \sum_{k=0}^{P} [F_k]\, \Psi_k(\boldsymbol{\xi}) = \sum_{\mathtt{u} \subseteq \mathcal{D}} F_\mathtt{u}(\boldsymbol{\xi}_\mathtt{u}), \quad F_\mathtt{u}(\boldsymbol{\xi}_\mathtt{u}) = \sum_{k \in \mathcal{K}(\mathtt{u})} [F_k]\, \Psi_k(\boldsymbol{\xi}),$$

where $\mathcal{K}(\mathtt{u}) \subseteq \{1, \cdots, P\}$ is the set of indices k for which $\Psi_k(\boldsymbol{\xi})$ is a polynomial of degree greater than zero $\boldsymbol{\xi}_\mathtt{u}$ and exactely zero in $\boldsymbol{\xi}_{\mathtt{u}_\sim}$:

$$k \in \mathcal{K}(\mathtt{u}) \Rightarrow \Psi_k(\boldsymbol{\xi}) = \Psi_k(\boldsymbol{\xi}_\mathtt{u}) \neq \Psi_0.$$

Consequently, the partial variance $\mathbb{V}\{F_\mathtt{u}\} = \sum_{k \in \mathcal{K}(\mathtt{u})} [F_k]^2$. Assuming such polynomial basis for the expan-

sion of X, we can derive the following expressions for the sensitivity indices of X:

$$\mathbb{V}\{X\}\,\mathtt{S}_{\mathtt{u}} = \sum_{k\in\mathcal{K}(\mathtt{u})} \mathbb{E}\left\{[X_k]\right\}^2, \quad \mathbb{V}\{X\}\,\mathtt{T}^{\mathrm{par}}_{\mathtt{u}} = \sum_{k\in\mathcal{T}(\mathtt{u})} \mathbb{E}\left\{[X_k]\right\}^2,$$
$$\mathbb{V}\{X\}\,\mathtt{T}^{\mathrm{mix}}_{\mathtt{u}} = \sum_{k\in\mathcal{T}(\mathtt{u})} \mathbb{V}\left\{[X_k]\right\}, \quad \mathbb{V}\{X\}\,\mathtt{T}^{\mathrm{mix}}_{\mathrm{noise}} = \sum_{\substack{\mathtt{u}\in\mathcal{D}\\ \mathtt{u}\neq\emptyset}} \sum_{k\in\mathcal{K}(\mathtt{u})} \mathbb{V}\left\{[X_k]\right\}, \tag{34}$$

where $\mathcal{T}(\mathtt{u}) \subseteq \{1,\cdots,P\}$ is the set of indices k such that Ψ_k is of degree > 0 in $\boldsymbol{\xi}_{\mathtt{u}}$.

When general bases are considered, *i.e.* not smooth polynomial bases as for instance with the multi-wavelet basis in Section 6, the computation of the sensitivity indices associated to $\mathtt{u}$ can be more involved (see for instance [40]) but remains essentially based on linear operators acting on the PC expansion, which can be efficiently implemented if the directional averages of the Ψ_k are known explicitly.

4.5. Computational Aspects

We now briefly discuss the computational procedure for estimating of the second-order characterization of X and its sensitivity analysis. Based on the discussion above, it is clear that this task essentially consists in computing the second order properties of the stochastic coefficient vector $\boldsymbol{X}$. The vector is governed by the coupled system of SODEs (13). Realizations of the stochastic vector can be obtained by solving (13) for a sample set $\mathcal{W} = \{W_j(t), j = 1,\ldots,M\}$ of M independent realizations of the Wiener process, resulting in a sample set $\mathcal{X} = \{\boldsymbol{X}_j(t), j = 1,\ldots,M\}$ of vector realizations. The usual (unbiased) estimators can be used to estimate the first and second moment of the vector,

$$\mathbb{E}\{\boldsymbol{X}\} \approx \widehat{\mathbb{E}\{\boldsymbol{X}\}} = \frac{1}{M}\sum_{j=1}^{M} \boldsymbol{X}_j, \quad [\mathbb{C}_{\boldsymbol{X},\boldsymbol{X}}] \approx \widehat{[\mathbb{C}_{\boldsymbol{X},\boldsymbol{X}}]} = \frac{1}{M-1}\sum_{j=1}^{M} \boldsymbol{X}_j^T\boldsymbol{X}_j - \widehat{\mathbb{E}\{\boldsymbol{X}\}}^T\,\widehat{\mathbb{E}\{\boldsymbol{X}\}}.$$

For a vanilla Monte-Carlo sampling, it is well known that the errors on the empirical estimators will decay as $1/\sqrt{M}$ such that a sufficiently large number of samples may eventually be needed for an accurate characterization of the process. This aspect can be improved, for instance by employing Multi-Level Monte-Carlo [13, 19], but we restrict in the following to basic MC sampling with low-order time-integration scheme, and focus on the PC decomposition.

5. System with Linear Drift

This section illustrates the implementation of the PC decomposition and the application of the orthogonal variance decomposition to quantify the impacts of stochastic forcing and uncertain parameters in the solution of SODEs with linear drift term. A case with non-linear drift term will be considered in section 6, treating a more complex model involving bifurcation near an unstable fixed point.

We start in section 5.1 by detailing the dynamics of the stochastic modes $[X]_k$ for a simple linear model with additive noise, namely the Ornstein-Uhlenbeck (OU) process with uncertain parameters. In section 5.2 we generalize the OU model to the case of multiplicative noise (drift coefficient depending on X) and highlight the impact of the multiplicative noise on the modes dynamics. In section 5.3 we illustrate the SH decomposition of the uncertain stochastic process into mean, parametric, noise and mixed components, in the multiplicative noise case, and finally report the the variance decomposition in section 5.4.

In the remainder of the section, we consider the model given by Equation (2) with the following generic forms of the drift and diffusion terms:

$$C(X,U) = Q_1 - X \qquad D(X,U) = (\nu X + 1)Q_2 \tag{35}$$

where Q_1 and Q_2 are independent, uniformly-distributed, random variables. This is symbolically expressed as $Q_i \sim \mathcal{U}[\mu_i, \sigma_i]$, where μ_i and σ_i respectively denote the mean and standard deviation of Q_i. Thus, in this

case we are dealing with a random parameter vector $U = (Q_1, Q_2)$. The Q_i's are parametrized in terms of canonical independent random variables ξ_i defined over the interval $[0, 1]$. The orthonormal PC basis consists of the appropriate tensorization of normalized Legendre 1D polynomials defined over the unit interval. We use for initial condition $X(t = 0) = 0$ almost surely, and so the PC expansion of the solution at $t = 0$ is given by $X_\alpha(t = 0) = 0\ \forall\alpha$. Note that for $\nu = 0$ a first-order expansion suffices to exactly represent $X(\xi)$.

The system of SODEs is then solved by means of Monte Carlo simulation for $t \in [0, 10]$ using the explicit Euler scheme (see Appendix A) with a time step $\Delta t = 0.01$.

5.1. Additive noise model

We start with the simple case of additive noise, $\nu = 0$, corresponding to the OU process with uncertain parameters, solution of

$$dX(\boldsymbol{\xi}) = (Q_1(\xi_1) - X(\boldsymbol{\xi}))dt + Q_2(\xi_2)dW.$$

Figure 1 shows typical paths (realizations) of $[X_\alpha]$ for the case $\nu = 0$, $\mu_1 = 1$, $\mu_2 = 0.1$, and $\sigma_1 = \sigma_2 = 0.05$. Only the first three expansion coefficients $[X_{k=0,1,2}]$ corresponding to polynomials Ψ_k with total degree less or equal to 1 are computed, as all higher order coefficients are zero. The solution is then sought as

$$X(t, U(\xi_1, \xi_2), \omega) = [X_0](t, \omega)\Psi_0 + [X_1](t, \omega)\Psi_1(\xi_1) + [X_2](t, \omega)\Psi_2(\xi_2),$$

where $\Psi_0 \doteq 1$. The plots show a sample set of trajectories of $[X_k](t, \omega)$ as well as their range of variability, depicted as the noise-averaged trajectories, $\mathbb{E}\{[X_k]\}(t)$, with $\pm$ 3 standard deviation bounds. For $[X_0]$ which corresponds to the zero-order term, that is the parametric-averaged process, an exponential like transition from 0 to the asymptotic value $\mathbb{E}\{Q_1\}$ with superposed random fluctuations are reported (see left plot). This dynamic is similar to the case of no-parametric uncertainty, with fluctuations induced by the noise, and can be explained by the governing equation of the mode:

$$d[X_0] = \left\langle Q_1(\xi_1) - \sum_{k=0}^{2}[X_k]\Psi_k, \Psi_0 \right\rangle dt + \langle Q_2(\xi_2), \Psi_0\rangle\, dW = (\mathbb{E}\{Q_1\} - [X_0])dt + \mathbb{E}\{Q_2\}\, dW.$$

In contrast, for $[X_1]$ in the center plot of Figure 1, which corresponds to the linear mode in ξ_1 (Q_1), no random fluctuations are seen. This is expected for the considered model as the mode is governed by a deterministic ODE, namely

$$d[X_1] = \left\langle Q_1(\xi_1) - \sum_{k=0}^{2}[X_k]\Psi_k, \Psi_1 \right\rangle dt + \langle Q_2(\xi_2), \Psi_1\rangle\, dW = (\langle Q_1(\xi_1), \Psi_1\rangle - [X_1])dt.$$

This shows that for this model, there is no interaction between the uncertainty in the drift term (Q_1) and the diffusion term (drift coefficient Q_2 and noise W_t). This property of the system may have been found out expanding the variance of X as a function of ξ_1 and ξ_2, to discover that it does not depend on ξ_1; however it would require many samples to accurately estimate the variance at various parameter values. In the present approach, on the contrary, this feature is immediately captured. Finally, one observes that trajectories for $[X_2]$, which accounts for the uncertainty in the diffusion coefficient, are centered and contain noise only. In fact, trajectories of $[X_2]$ obey the damped diffusion process:

$$d[X_2] = \left\langle Q_1(\xi_1) - \sum_{k=0}^{2}[X_k]\Psi_k, \Psi_2 \right\rangle dt + \langle Q_2(\xi_2), \Psi_2\rangle\, dW = -[X_2]dt + \langle Q_2, \Psi_2\rangle\, dW.$$

5.2. Multiplicative noise

We now consider a case with $\nu \neq 0$. In this situation, the diffusion term involves a product between the state, X, and the Wiener process, W, with a more complicated solution structure as a result. The Galerkin procedure is applied here with a polynomial truncation at total order $\mathrm{N_o} = 5$. The total number

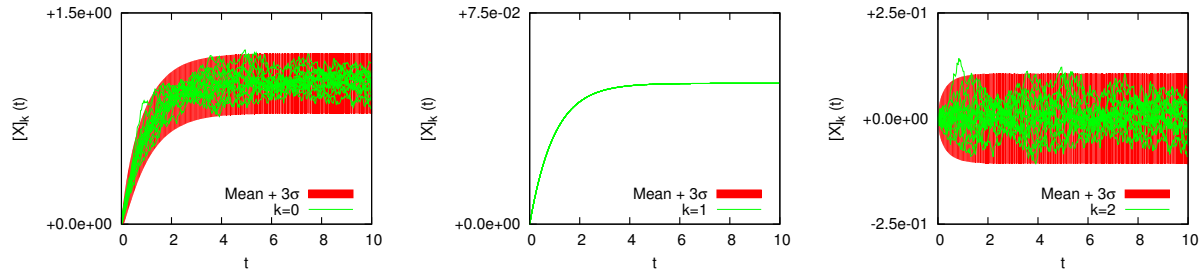

Figure 1: Sample set of few trajectories and variability ranges for the three coefficients $[X_k](t,\omega)$ of the solution of the model defined by (35). An additive noise model is assumed, with $\mu_1 = 1$, $\mu_2 = 0.1$, $\sigma_1 = \sigma_2 = 0.05$, and $\nu = 0$. The plots correspond to $k = 0$, 1 and 2, arranged from left to right.

of modes in the solution expansion is then $P + 1 = 21$. We compute a total of 50,000 trajectories that are subsequently used to estimate the W-averages of the $[X_k]$ and their second moments. From these first and second moments, the partial and conditional variances can be estimated.

Figure 2 shows typical paths (realizations) of $[X_k]$ for $\nu = 0.2$; the remaining parameters are identical to those in Fig. 1. Only coefficients up to order 4 are shown, with total order increasing from top to bottom and order in ξ_1 decreasing from left to right. It is seen that the paths of $[X_0]$ (top plot) and $[X_2]$ (second row, right plot) have a structure similar to those shown for the previous (additive) linear model. However, $[X_1]$ (second row, left plot) now exhibits fluctuations, as one may have expected from the dependence of the diffusion term on X. For the higher order terms, we remark that only coefficients associated to polynomials with degree less or equal to 1 in ξ_1 are non vanishing, owing to the structure of the uncertainty model. Indeed, $Q_2(\xi_2)$ having non-vanishing components along Ψ_0 and Ψ_2 only, that is $Q_2 = \mu_2\Psi_0 + \sigma_2\Psi_2$, the projection of the diffusion term on Ψ_k becomes

$$\begin{aligned} D_k &= \nu \left\langle Q_2 \sum_l [X_l]\Psi_l, \Psi_k \right\rangle + \langle Q_2, \Psi_k \rangle \\ &= \nu\mu_2 \sum_l [X_l] \langle \Psi_l, \Psi_k \rangle + \nu\sigma_2 \sum_l [X_l] \langle \Psi_l\Psi_2, \Psi_k \rangle + \mu_2 \langle \Psi_0, \Psi_k \rangle + \sigma_2 \langle \Psi_2, \Psi_k \rangle \\ &= \nu\mu_2 \sum_l [X_k] + \nu\sigma_2 \sum_l [X_l] \langle \Psi_l\Psi_2, \Psi_k \rangle \, \mu_2\delta_{0k} + \sigma_2\delta_{2k}, \end{aligned} \tag{36}$$

and the initial conditions being $[X_k] = 0$ for all k, we see that only a subset of coefficients are susceptible to grow due to the diffusion term.

We note from Figure 2 the fast decay in the magnitude of the non-vanishing coefficients $[X_k]$, which demonstrates the convergence of the PC expansion of X. We also note that some low order coefficients have distributions that appear roughly symmetric about the mean value, while high-order ones tend to exhibit long tails, reflecting the symmetry breaking of the multiplicative diffusion term. This can be better appreciated from the plots of Figure 3, which depict the estimated marginal probability density functions of some of the coefficients $[X_k]$ at time $t = 10$. The densities are estimated using classical Kernel-density-estimation (KDE) based on a Gaussian kernel and using a large sample set of 100,000 MC realizations. We observe that modes $k = 0, 1, 2$ and 4 indeed follow an essentially Gaussian distribution (with a small skewness toward higher values) while the other modes affected by the noise have significantly skewed distributions. Further, normalized distributions for $[X_5]$ and $[X_8]$, and $[X_9]$ and $[X_{13}]$, are indistinguishable. The similar densities between some of the modes $[X_k](t,\omega)$ is explained by the structure of the system, which induces complete dependences between them, namely affine relations.

To better appreciate the dependence between the modes $[X_k]$, we provide in Figure 4 samples of the 2D projection for the centered and (component-wise) normalized vector $\boldsymbol{X}(t,\omega)$ at $t = 10$. Specifically, the plots show realizations of (normalized) $[X_k]$ versus $[X_{k'}]$, for some couples (k, k') to illustrate the underlying dependences between components. Whenever the realizations align on the $x = y$ axis, an affine relation between $[X_k]$ and $[X_{k'}]$ can be inferred. This is presently the case for any of couple (k, k') where $[X_k]$ and

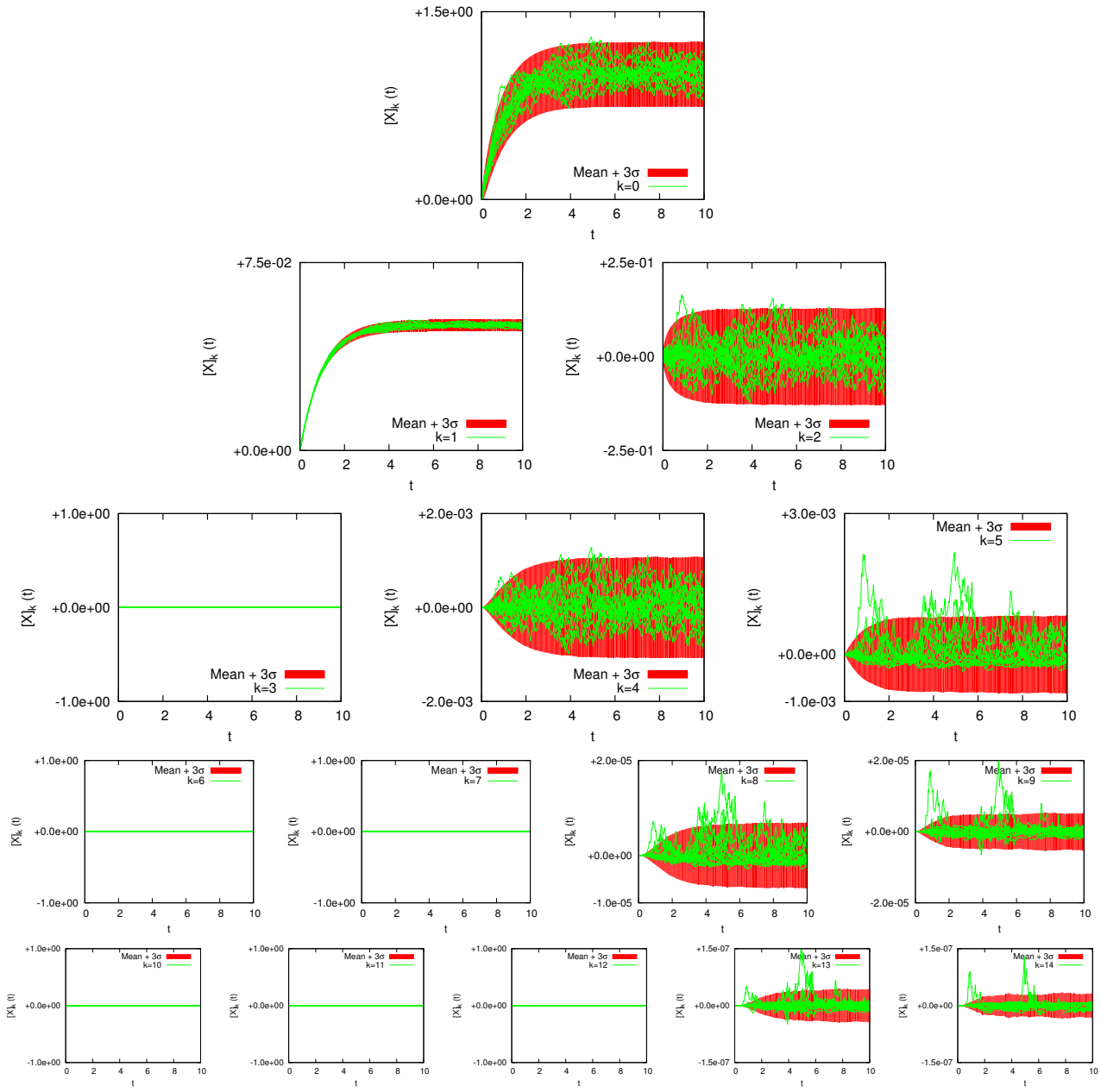

Figure 2: Sample trajectories of $[X_k]$, $0 \leq k \leq 14$. The total order ranges from 0 (top row) to 4 (bottom row), with and decreasing order in ξ_1 from left to right. A multiplicative noise model is assumed, with $Q_1 \sim \mathcal{U}[1, 0.05]$, $Q_2 \sim \mathcal{U}[0.1, 0.05]$, and $\nu = 0.2$.

$[X_{k'}]$ have the same reduced distribution. Therefore, Figure 4 only depicts the realizations for couples based on indices corresponding to distinct types of distributions, namely for couples based on the indices $k = 0$, 5, 9 and 14. The structures in the projections plotted in Figure 4 highlight the strong dependences between the modes and reflect their non-linear coupling. In fact, the stochastic solution vector $\boldsymbol{X}(t, \omega)$ belongs to a low-dimensional manifold of $\mathbb{R}^{P+1}$ which converges asymptotically at large time, as the stochastic vector converges to its asymptotic distribution.

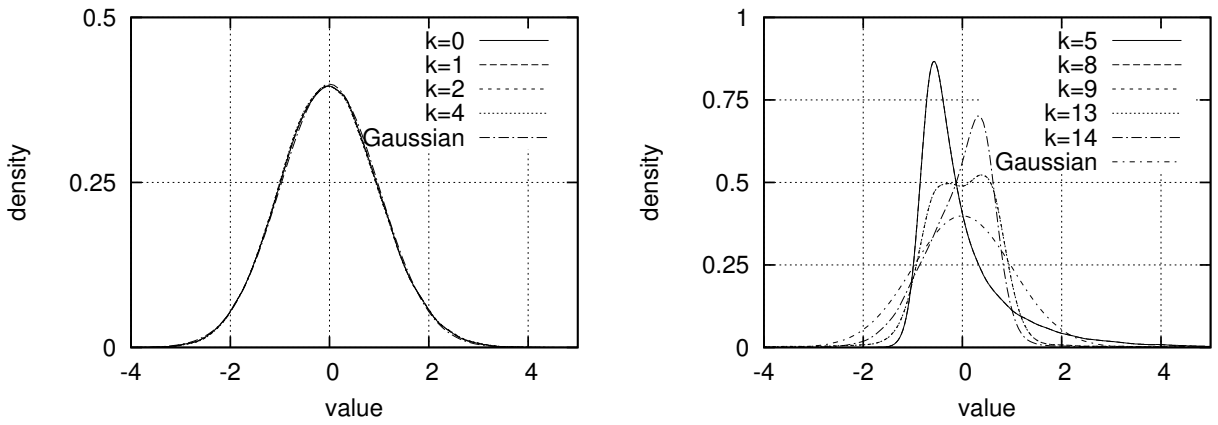

Figure 3: Probability density functions of the modes $[X_k]$ at $t = 10$. The modes have been centered and normalized to facilitate the comparison; the standard Gaussian distribution is also reported for reference. A multiplicative noise model is assumed, with $Q_1 \sim \mathcal{U}[1, 0.05]$, $Q_2 \sim \mathcal{U}[0.1, 0.05]$, and $\nu = 0.2$.

5.3. SH decomposition of X

We now apply the SH decomposition of X in parametric, noise and mixed contributions, based on results obtained for the previous model with $\nu = 0.2$. Figure 5 (left) shows samples of X trajectories for different $\boldsymbol{\xi}(\omega)$ and a *fixed* realization of the noise W; conversely, the right plot depicts trajectories of X for different realizations of the noise at a *fixed* value of the parameters. These plots illustrate how the uncertain parameters and the noise affect the process in a different fashion. In contrast to the variability due to the noise W, all realizations in the left plot have a similar structure in their fluctuations when varying the parameters.

Figure 6 illustrates the SH decomposition of X into X_{par}, X_{noise} and X_{mix}. Starting from a sample set of trajectories of $X(\omega)$ (top left), the top right and bottom left plots respectively show the corresponding realizations of the conditional expectations, $\mathbb{E}\{X \mid \boldsymbol{\xi}(\omega)\} = \bar{X} + X_{\text{par}}(\boldsymbol{\xi}(\omega))$ and $\mathbb{E}\{X \mid W(\omega)\} = \bar{X} + X_{\text{noise}}(W(\omega))$. It is seen that X_{par} and X_{noise} have dramatically different characters: while X_{par} is smooth in time, X_{noise} exhibits substantial fluctuations (in fact, realizations are nowhere differentiable in t). Finally, the bottom right plot depicts the corresponding trajectories of the mixed contribution X_{mix}, which is interpreted as a correction, depending on $\boldsymbol{\xi}$, of the intrinsic fluctuations in X_{noise}.

In Figure 7, we provide the surface response with respect to the model parameters of the conditional mean and variance of X at $t = 10$. The left (resp. right) plot shows $\mu_X(\boldsymbol{\xi}) - \mathbb{E}\{X\} = X_{\text{par}}(\boldsymbol{\xi})$ (resp. $\Sigma^2_X(\boldsymbol{\xi})$) given by (19) (resp. (20)). For clarity, the horizontal axes show the values of the drift $Q_1(\boldsymbol{\xi})$ and diffusion $Q_2(\boldsymbol{\xi})$ parameters. It is observed that the local W-average of X essentially depends only on the drift parameter $Q_1(\boldsymbol{\xi})$. In contrast, the W-variance of X depends predominantly on the uncertain diffusion coefficient $Q_2(\boldsymbol{\xi})$.

5.4. Analysis of the variance

Figure 8 shows the partial variances V_{par}, V_{noise} and V_{mix} and the total variance $\mathbb{V}\{X\}$ for the multiplicative model with parameters $Q_1 \sim \mathcal{U}[1, \sigma_1]$, $Q_2 \sim \mathcal{U}[0.1, \sigma_2]$, and $\nu = 0.2$. Four cases are contrasted. The top-left panel corresponds $\sigma_1 = \sigma_2 = 0$, *i.e.* the case of a model having no parametric uncertainty. As a result, all partial variance terms except V_{noise} are zero, and the only variability in the SODE solution is due to the stochastic nature of W. The bottom left panel corresponds to $\sigma_1 = 0.05$ and $\sigma_2 = 0$, so the diffusion coefficient is deterministic. In this case, the W-averaged asymptotic solution, $\mathbb{E}\{X \mid W\}$, is clearly subject to parametric uncertainty such that, in addition to V_{noise}, V_{par} is also non zero. However, the variance of the mixed term V_{mix} remains several order of magnitude lower that the other partial variances; in other words, there is negligible joint effect of the noise and parametric uncertainty. On the contrary, the cases $\sigma_1 = 0$ and $\sigma_2 = 0.05$ (top-right) lead to a vanishing partial variance V_{par} and a significant mixed variance V_{mix}. Indeed, in the absence of noise the solution would be deterministic, and the uncertainty in the model parameters only intervenes in the diffusion coefficient, which triggers the mixed term. Finally, for $\sigma_1 = \sigma_2 = 0.05$

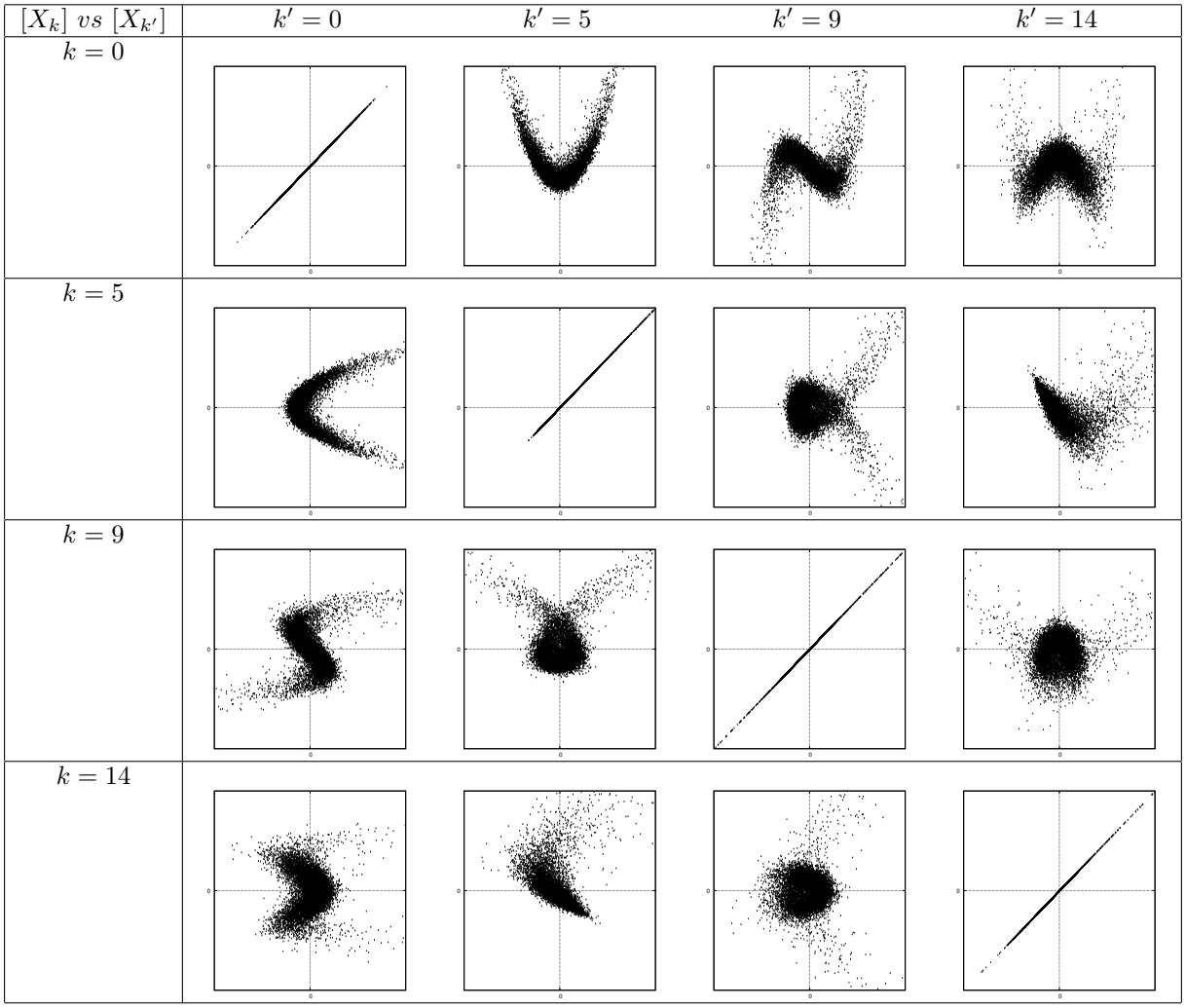

Figure 4: Projections in the planes $([X_k], [X_{k'}])$ of realizations of the centered and normalized solution vector $\boldsymbol{X}$ at time $t = 10$, for selected indices k and k' as indicated. A multiplicative noise model is assumed, with $Q_1 \sim \mathcal{U}[1, 0.05]$, $Q_2 \sim \mathcal{U}[0.1, 0.05]$, and $\nu = 0.2$.

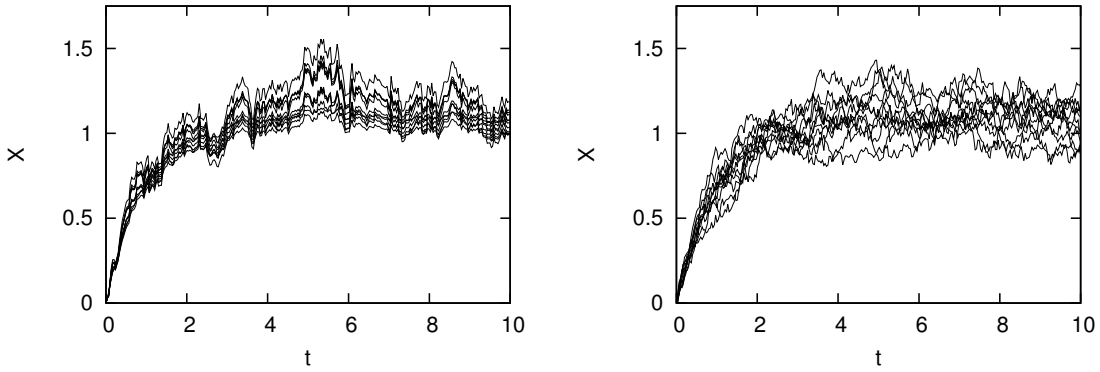

Figure 5: Samples of trajectories of X computed using the PC expansion. The left plot shows trajectories for samples of $\boldsymbol{\xi}$ and a *fixed* realization of W. The right plot shows trajectories for samples of W at a *fixed* value of the parameters. A multiplicative noise model is assumed, with $Q_1 \sim \mathcal{U}[1, 0.05]$, $Q_2 \sim \mathcal{U}[0.1, 0.05]$, and $\nu = 0.2$.

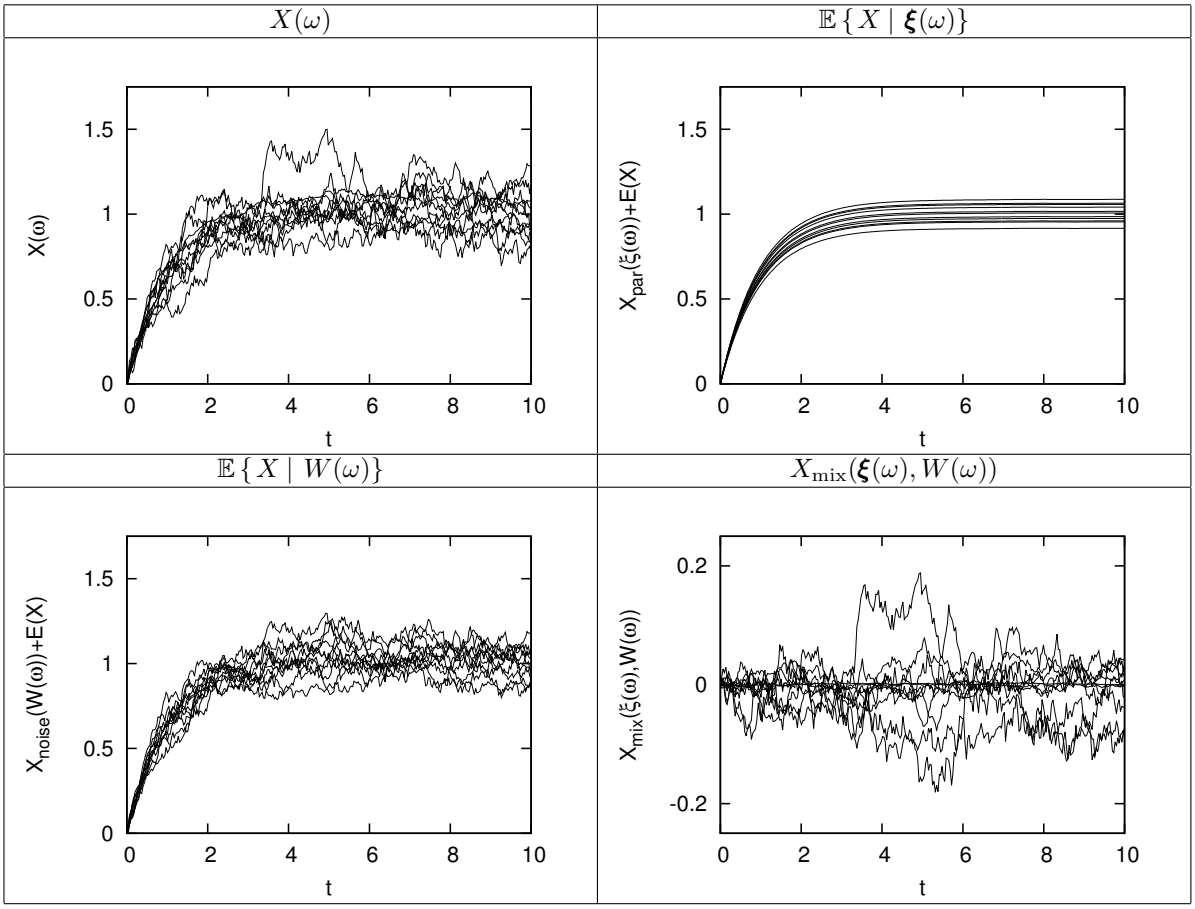

Figure 6: Sample set of trajectories of X and its SH functions, computed using the PC expansion. The top left plot shows trajectories $X(\omega)$. The top right and bottom left plots show the corresponding trajectories of $X_{\mathrm{par}}(\boldsymbol{\xi}(\omega)) + \mathbb{E}\{X\}$ and $X_{\mathrm{noise}}(W(\omega)) + \mathbb{E}\{X\}$. The bottom right plot shows the realizations of $X_{\mathrm{mix}}(\boldsymbol{\xi}(\omega), W(\omega))$. A multiplicative noise model is assumed, with $Q_1 \sim \mathcal{U}[1, 0.05]$, $Q_2 \sim \mathcal{U}[0.1, 0.05]$, and $\nu = 0.2$.

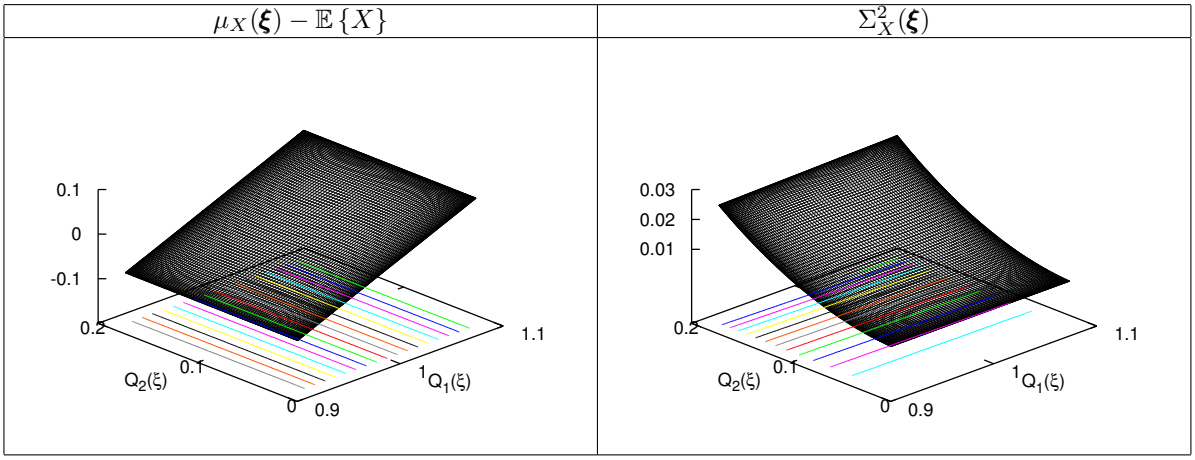

Figure 7: Dependence with respect to the model parameters $Q_1(\boldsymbol{\xi})$ and $Q_2(\boldsymbol{\xi})$ of the (centered) conditional mean $\mu_X(\boldsymbol{\xi}) = \mathbb{E}\{X \mid \boldsymbol{\xi}\} - \mathbb{E}\{X\}$ and variance $\Sigma^2_X(\boldsymbol{\xi}) = \mathbb{V}\{X \mid \boldsymbol{\xi}\}$ at time $t = 10$. A multiplicative noise model is assumed, with $Q_1 \sim \mathcal{U}[1, 0.05]$, $Q_2 \sim \mathcal{U}[0.1, 0.05]$, and $\nu = 0.2$.

(bottom-right) all the partial variances become non-zero. In fact, for this setting V_{par} and V_{mix} have similar values, while the partial variance V_{noise}, due to W alone, remains the dominant contributor to the total

variance. The increase in the total variance as more parametric uncertainties are introduced can also be appreciated from these plots.

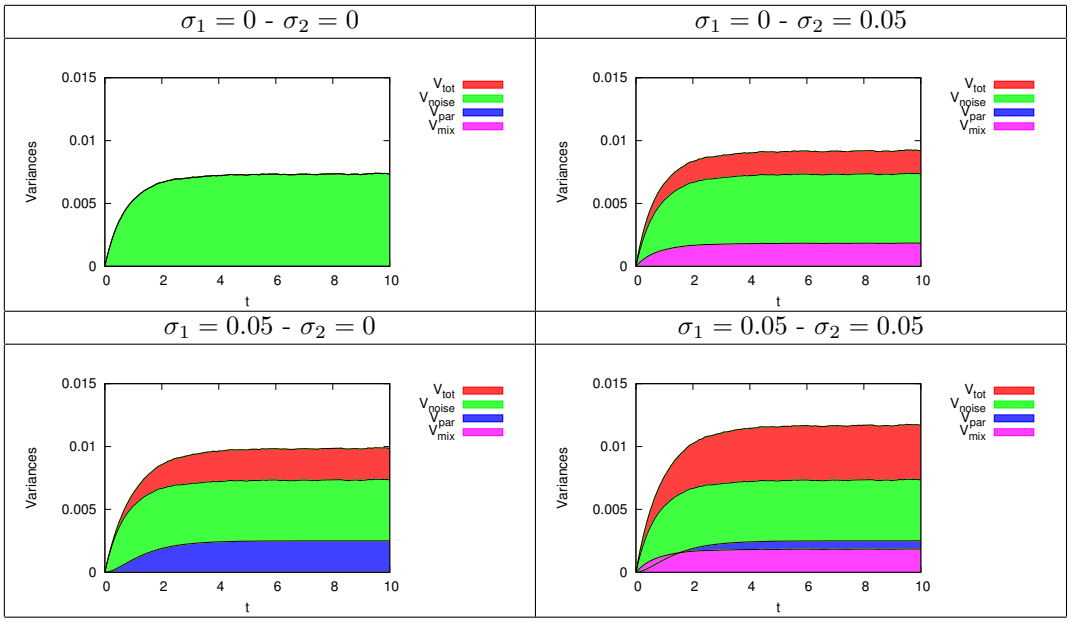

Figure 8: Evolution of the components of the total variance. A multiplicative noise model is assumed, with $Q_1 \sim \mathcal{U}[1, \sigma_1]$ and $Q_2 \sim \mathcal{U}[0.1, \sigma_2]$, and $\nu = 0.2$. Shown are decompositions obtained for different values of the standard deviations σ_1 and σ_2, as indicated.

In order to gain additional insight into the effect of the mean diffusion coefficients, additional computations are performed, namely by fixing $\mu_1 = 1$, $\sigma_1 = 0.1$, $\sigma_2 = 0.05$, $\nu = 0.2$, and varying μ_2; specifically, we use $\mu_2 = 0.1$, 0.2 and 0.3. The partial variances obtained for all three cases are reported in Figure 9. The results shows that, with all other parameters fixed, the intrinsic contribution of the noise W to the solution variability becomes increasingly important as the mean value of the diffusion coefficient increases. On the contrary, the purely parametric part X_{par} as well as the mixed contribution X_{mix} have constant magnitude, highlighting the constant variability in the model parameters in all the three cases.

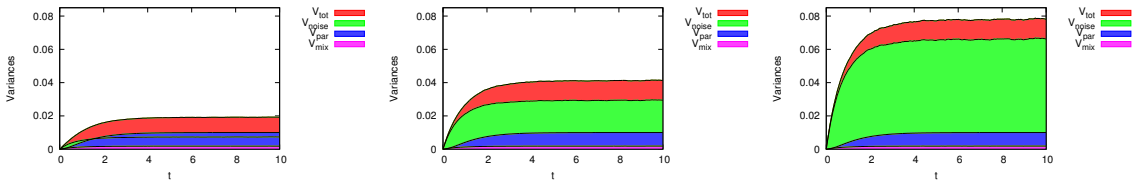

Figure 9: Evolution of the components of the total variance. A multiplicative noise model is assumed, with $Q_1 \sim \mathcal{U}[1, 0.05]$ and $Q_2 \sim \mathcal{U}[\mu_2, 0.05]$, and $\nu = 0.2$. Shown are variance decompositions obtained for different values of the mean of the diffusion coefficient μ_2. Left: $\mu_2 = 0.1$; center: $\mu_2 = 0.2$; right: $\mu_2 = 0.3$.

We conclude these section by remarking that the proposed decomposition of the variance could be refined to assess separately the respective contributions to the variance of the individual components of the germ, ξ_1 and ξ_2. This would allow us to hierarchize the effects of the parametric uncertainties in the drift and diffusion coefficients. Such study is not presented here as the results are immediate, namely because the mixed contribution always depends only marginally on the drift parameter Q_1 (ξ_1).

6. Stochastic Bifurcation Problem

We now consider a more complex system, starting from the deterministic ODE

$$\frac{dx}{dt} = F(x), \quad F(x) = -\gamma(x-a)(x-b)(x-c) \tag{37}$$

where a, b, c and γ are known parameters satisfying $0 < a < b < c$, and $\gamma > 0$. The ODE is completed with the initial condition, $x^0 \equiv x(t=0)$. A straightforward analysis reveals that the dynamics exhibit three fixed points $x = a$, $x = b$, and $x = c$, the second fixed point $x = b$ being unstable.

Figure 10 depicts trajectories of the deterministic system starting from different initial conditions for the values $a = 10, b = 20, c = 30$ and $\gamma = 0.01$. The results illustrate that when $x^0 > c$ the system rapidly approaches the stable fixed point $x = c$, and when $x^0 < a$ the system rapidly approaches the stable fixed point $x = a$. Meanwhile, starting the neighborhood of $x = b$, the system will diverge towards $x = c$ or $x = a$, according to whether $c > x^0 > b$ or $a < x^0 < b$.

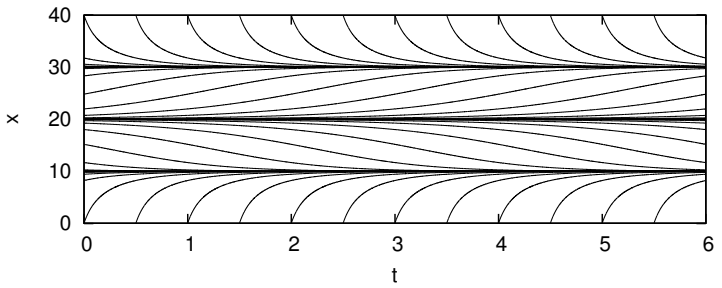

Figure 10: Sample trajectories for the deterministic model system (37), starting from different initial conditions. Solutions are obtained using $a = 10$, $b = 20$, $c = 30$ and $\gamma = 0.01$.

A stochastic variant of the above deterministic system is considered next, namely by including an additive stochastic forcing term, leading to the SODE

$$dX = F(X)dt + \delta dW = -\gamma(X-a)(X-b)(X-c)dt + \delta dW, \tag{38}$$

where $\delta > 0$ is an additional parameter controlling the noise level, and as before W is a Wiener process. The SODE is again completed by an initial condition $X^0 = X(t=0)$.

Figure 11 depicts trajectories of the stochastic system governed by (38), all starting from the deterministic initial condition, $X(t=0) = b$. These trajectories are obtained using $a = 10$, $b = 20$, $c = 30$ and $\delta = 1$. The results indicate that, due the stochastic forcing, the point $x = b$ is no longer a fixed point of the system, and that the stochastic system is rather characterized by two attracting branches, $x = a$ and $x = c$. After a transient time, $X(t)$ selects one of the two attracting branches and asymptotically fluctuates around it (with a very low probability of switching from one attracting branch to another). Here, because of the symmetric settings of the model, there is an equal probability to select one or the other attracting branch.

6.1. Parametric uncertainty

To analyze the combined effect of parametric uncertainty and stochastic forcing, we extend the formulation by considering two independent uncertain parameters, characterizing the initial condition, X^0, and the forcing amplitude, δ. Specifically, we set $X^0 \sim \mathcal{R}[17.5, 22.5]$ and $\delta \sim \mathcal{R}[0.5, 1.5]$, where $\mathcal{R}[x, y]$ denotes the uniform distribution over the range $[\min(x, y), \max(x, y)]$. The other parameters of the system are held fixed to $a = 10$, $b = 20, c = 30$ and $\gamma = 0.01$ throughout the rest of the section. The uncertain parameters X^0 and δ are respectively parameterized by independent canonical uniform random variables ξ_1 and ξ_2, both defined over the unit interval $[0, 1]$, such that

$$X^0 = X^0(\xi_1), \quad \delta = \delta(\xi_2), \quad \boldsymbol{\xi} = (\xi_1, \xi_2) \in \Xi = [0,1]^2, \quad p_{\boldsymbol{\xi}}(\boldsymbol{x}) = \begin{cases} 1 & \boldsymbol{x} \in \Xi \\ 0 & \text{otherwise} \end{cases}.$$

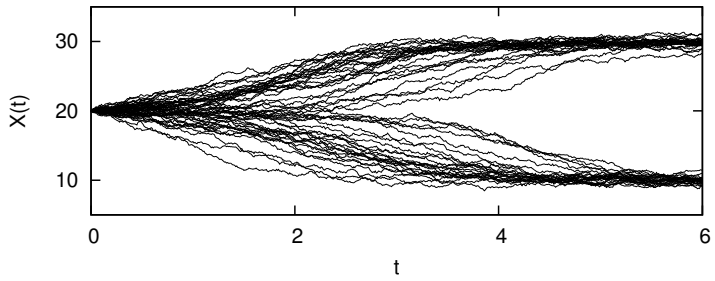

Figure 11: Sample trajectories for the model system (38), with $a = 10$, $b = 20$, $c = 30$, $\gamma = 0.01$, and $\delta = 1$. In all cases, the initial condition coincides with $x^0 = b$, namely the unstable fixed point of the corresponding deterministic system.

In Figure 12, we start by illustrating the dynamics of the system when the uncertain parameters vary, namely by plotting the evolution of the state, X, for selected realizations of the uncertain parameters $X^0(\xi_1)$, $\delta(\xi_2)$, and for a set of realizations for the Wiener process. The two plots at the left of Figure 12 depict trajectories of X for different realizations of the noise, using 7 different deterministic initial conditions distributed in the range $[17.5, 22.5]$ and two noise levels $\delta = 0.65$ (top) and $\delta = 1.35$ (bottom). For these two plots, time runs up while $X(t)$ is reported along the horizontal axis, with a shift to separate the cases of different initial conditions (the unstable point b is reported for reference). It is seen that when X^0 is far from b, the trajectories are going to the closest attracting branch with high probability. On the contrary, when X^0 comes closer to b, the noise is able to drive X toward the farthest attracting branch with increasing probability. In addition, comparing the top and bottom plots, it can be seen that the higher the noise level, the higher the probability to reach the farthest attracting branch (though it never exceeds the probability of selecting the closest).

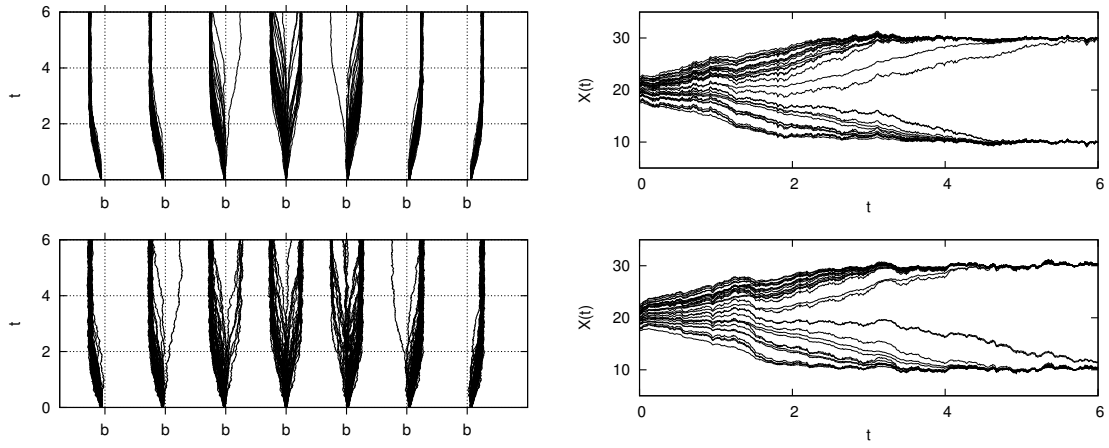

Figure 12: Sample trajectories for the model system (38), with $a = 10$, $b = 20$, $c = 30$, and $\gamma = 0.01$. The left plots show for a sample set of realizations of W, the trajectories of X (time running up) for different deterministic initial conditions equally distributed around b in the range $[17.5, 22.5]$ and two noise levels $\delta = 0.65$ (top plot) and $\delta = 1.35$ (bottom). The right plots show for two realizations of W (top and bottom), the corresponding trajectories of X for a random sample set of values of X^0 and δ in their uncertainty range.

Shown in each of the two plots at the right of Figure 12 are trajectories of a fixed realization of the Wiener process but a random sample set of the parameters X^0 and δ. Again, trajectories that start away from the unstable point $x = b$ tend to be rapidly attracted towards the closest attracting branch. On the other hand, realizations starting close to $X = b$ may be attracted towards either attracting branch. As for the linear drift problems above, it is seen that, with W held fixed, the noise introduces small scale fluctuations that are highly correlated as the parameters change. However, due to the bifurcation in the system, the continuity of X with respect to the uncertain parameters is lost as t increases. This is evidenced by the absence of trajectories in between the two attracting branches for large enough time.

6.2. Stochastic Multi-Resolution Scheme

As remarked above, the bifurcation induces a loss of continuity of X with respect to the random parameters. This characteristic prevents us from using a PC expansion, $X(t,\omega) = \sum_k [X_k](t,\omega)\Psi_k(\boldsymbol{\xi})$, on classical spectral polynomial basis, $\{\Psi_k, k \in \mathbb{N}\}$, because of slow convergence and Gibbs phenomena in truncated simulations. To tackle the potential lack of regularity in the solution, given W, we consider a stochastic multi-wavelet (MW) discretization [22, 24] of X in the uncertain parameters, instead of a smooth polynomial approximation. The MW basis consists in the tensorization of Alpert's hierarchical basis [2] and results in a piecewise polynomial approximation over a uniform partition of Ξ. The MW basis is hierarchical in the sense that it consists of mutually orthogonal functionals corresponding to details at different scales.

The discretization is controlled by two parameters, the resolution level, Nr, and the polynomial order, No. Specifically, $\mathrm{Nr} \geq 0$ controls the finest scales of details in the hierarchy. It corresponds to a piecewise approximation over subdomains resulting from Nr recursive dyadic partitions of Ξ along each of its dimension. For the present problem with 2 independent random variables, $\boldsymbol{\xi} = (\xi_1, \xi_2)$, the domain Ξ is partitioned into $2^{2\mathrm{Nr}}$ non-overlapping subdomains (squares) having equal size. Meanwhile, $\mathrm{No} \geq 0$ controls the polynomial order of the approximation over each of the subdomains. The situation with $\mathrm{No} = 0$ corresponds to the so-called Wiener-Haar expansion of X (see [22]). Overall, the total dimension of the MW space in our 2D problem is $2^{2\mathrm{Nr}}(\mathrm{No}+1)^2$ which becomes very large as No and Nr are increased. The approximation can be expressed as

$$X(t,\omega) = \sum_{k \in S_{\mathrm{Nr,No}}} [X_k](t,\omega)\Psi_k(\boldsymbol{\xi}),$$

where $S_{\mathrm{Nr,No}}$ is the set of MW indices and Ψ_k are now the orthonormal MW basis functions.

To maintain a reasonable computational complexity an adaptive procedure is needed (see [25]). The adaptive procedure exploits the facts that the initial condition is smooth (in fact linear in ξ_1) and that the solution may develop in time a bifurcation which is however localized in Ξ for a given realization of W. As a result, for each realization of the noise, the corresponding solution has a sparse representation in the MW basis since most details are negligible, i.e. $X(t)$ is compressible in the MW basis. In the present work, we rely on a multi-resolution scheme following the anisotropic adaptive strategy introduced in [40]. The principle of the adaptive strategy is quite simple and consists in constructing, for each sample of $W(\omega)$, subsets of active MW indices $S^i(\omega) \subseteq S_{\mathrm{Nr,No}}$ at every time $t = i\Delta t$; the approximation thus becomes

$$X(t = i\Delta t, \omega) \approx X^i(\omega) = \sum_{k \in S^i(\omega)} [X_k]^i(\omega)\Psi_k(\boldsymbol{\xi}).$$

Starting from an initial coarse set $S^0(\omega) = S_{1,\mathrm{No}}$, which allows here for an exact representation of the initial condition if $\mathrm{No} \geq 1$, we defined recursively the (random) sequence of sets $S^0(\omega) \mapsto S^1(\omega) \mapsto S^2(\omega) \mapsto \cdots$, by successive enrichments (completions), that is $S^{i+1}(\omega) \supseteq S^i(\omega)$, constrained by $S^{i+1}(\omega) \subseteq S_{\mathrm{Nr,No}}$. Practically, we rely on the directional enrichment indicator proposed in Section 4.2 of [40] to enrich $S^i(\omega)$ to $S^{i+1}(\omega)$. Essentially, the directional enrichment indicator checks the decay rates of the MW coefficients along each ξ_i to decide the introduction of additional detail basis functions in the discretization. Figure 13 illustrates the adaptation of the MW expansion of X for $\mathrm{Nr} = 6$. It presents for 2 realizations of W the adapted MW discretizations at the final time, $t = 6$. The discretizations are plotted as the partitions of Ξ into subdomains supporting smooth polynomial approximations, here set to $\mathrm{No} = 2$. On the right of the partitions, the corresponding realization of the surface response of X are plotted as function of $X^0(\xi_1)$ and $\delta(\xi_2)$. The figure illustrates how the adaptive strategy refines the MW space in areas of Ξ where X exhibits a bifurcation with steep dependence with respect to $\boldsymbol{\xi}$.

Note first that the enrichment is applied at every time iteration, owing to a low computational cost, when the discretization in fact mostly evolves during the transient stage only, and not much after the attracting branch has been selected. Second, the dimension of the MW basis monotonically grows as there is no coarsening step in the adaptation. This is justified again by the present dynamics of the system, because the location of the bifurcation in the Ξ domain does not evolve after the selection of the attracting branch, owing to the large separation $c - a$ relative to the size of Wiener fluctuations (controlled by δ), which makes branch-switching very unlikely (in fact never observed in our simulations). This point is illustrated

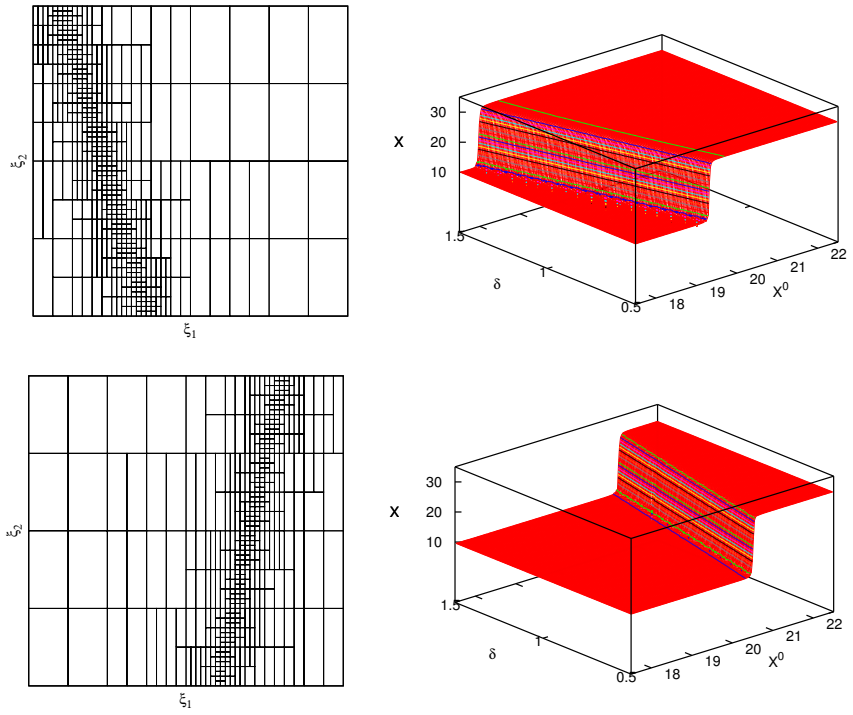

Figure 13: Illustration of the adaptive MW computations for two realizations $W(\omega)$ of the noise (top and bottom). The plots show for $t = 6$ the partitions of Ξ into subdomains supporting smooth polynomial approximations, and the surface plots of the corresponding approximations of $X(t = 6, \omega)$ as a function of $X^0(\xi_1)$ and $\delta(\xi_2)$. The results are obtained using a MW approximation with $\mathrm{Nr} = 6$, $\mathrm{No} = 2$, and parameters $X^0 \sim \mathcal{R}[17.5, 22.5]$ and $\delta \sim \mathcal{R}[0.5, 1.5]$.

in Figure 14 which shows, for two realizations of the noise, the surface responses of $X(t, \omega)$ as function of $X^0(\xi_1)$ and $\delta(\xi_2)$, at time $t = 1$, $t = 3$ and $t = 6$. These plots show that when the attracting branch is selected, the dynamics reduces to surface responses exhibiting dependences with respect to the parameters that become steeper as time increases; this behavior reflects the decreasing probability of having $X \approx b$. The plots also indicate that simulations for longer times would require an increasing resolution level Nr as X is asymptotically discontinuous. However, for the present settings, numerical tests have shown that $\mathrm{Nr} = 6$ was enough to have a sufficient accuracy in the neighborhood of the bifurcation up to $t = 6$, especially in light of the error due to the finite sampling of W.

As a consequence of the adaptive MW discretization, realizations of the discrete process X^i are known as functions of $\boldsymbol{\xi}$ over subspaces $S^i(\omega)$ depending on the noise $W(\omega)$. However, these realizations of X^i can be eventually projected (in fact, injected) in $S_{\mathrm{Nr,No}}$ defining

$$X(t = i\Delta t, \omega) \approx X^i(\omega) = \sum_{k \in S_{\mathrm{Nr,No}}} [X_k]^i(\omega) \Psi_k(\boldsymbol{\xi}), \quad [X_k]^i(\omega) = \begin{cases} [X_k]^i(\omega) & k \in S^i(\omega), \\ 0 & \text{otherwise.} \end{cases}$$

Doing so, and using $\Psi_0 = 1$, we are back to the assumptions of Section 4 and the analysis can be performed as previously.

6.3. Analysis of the variance

Based on a sampling of W, we generate samples of the stochastic MW coefficients that are used to perform the Sobol decomposition of X and the analysis of the variance. The following results use a sample set to 20,000 independent trajectories of the Wiener process, and a 2nd order Runge-Kutta scheme for the time discretization of the system of SODEs for the MW coefficients (see Appendix A) with $\Delta t = 0.01$. As

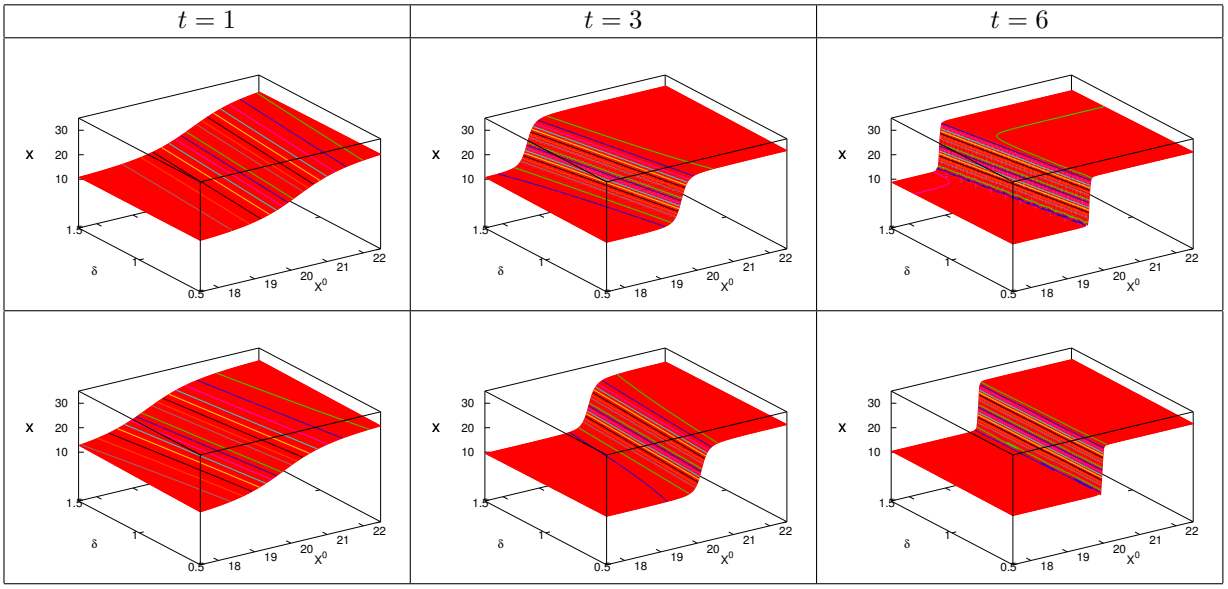

Figure 14: Responses surfaces of $X(t,\omega)$ as function of $X^0(\xi_1)$ and $\delta(\xi_2)$ at time $t = 1$, 3 and 6 as indicated, and for two realizations of the noise (top and bottom rows). The computations use an adaptive MW discretization with $S_{\mathrm{Nr,No}}$, $\mathrm{Nr} = 6$ and $\mathrm{No} = 2$, and uncertain system parameters $X^0 \sim \mathcal{R}[17.5, 22.5]$ and $\delta \sim \mathcal{R}[0.5, 1.5]$.

mentioned previously, computations use $\mathrm{Nr} = 6$ and $\mathrm{No} = 2$ for the adaptive multi-wavelet discretization of each noise realization.

We start by analyzing in Figure 15 the conditional expectations $\mathbb{E}\{X \mid \boldsymbol{\xi}\} = X_{\mathrm{par}}(\boldsymbol{\xi}) + \mathbb{E}\{X\}$. Focusing first on the response surface plots of the conditional expectation at $t = 1, 3$ and 6 (top row) it is seen that, contrary to the case of individual realizations of the noise (see plots of Figure 14 for comparison) the $\boldsymbol{\xi}$-dependence of $\mathbb{E}\{X \mid \boldsymbol{\xi}\}$ remains smooth. This reflects the averaged effect of the noise which, by moving the bifurcation, smoothes it out. This is also illustrated in the bottom plot of Figure 15, which depicts trajectories of the conditional expectation for a random sample set of $\boldsymbol{\xi}$. This plot, which should be contrasted with the two individual W-realizations in the left plots of Figure 12, is populated in between the two attracting branches, because for a fixed value of $\boldsymbol{\xi}$ one or the other branch may be selected depending on W, and so on average it lies in between. These results also point that the W-average of the MW coefficients vector $\boldsymbol{X}(t,\omega)$ is very sparse and could be computed in a MW space of low resolution with significant computational savings (although computation of individual realizations requires sufficiently large Nr).

Figure 16 depicts the conditional variance $\mathbb{V}\{X \mid \boldsymbol{\xi}\} = \Sigma^2_X(\boldsymbol{\xi})$ for three different times $t = 1, 3$ and 6. Again, the conditional variance is plotted as function of the uncertain parameters $X^0(\xi_1)$ and $\delta(\xi_2)$. We observe that irrespective to the initial condition, the W-variance of X increases with δ as one would expect. However, for $t \geq 3$ the variance conditioned on $\boldsymbol{\xi}$ has a magnitude, particularly for initial conditions around b, exceeding by far the amount suggested by the fluctuations around each of the branches reported in Figure 11. This is again explained by the effect of the noise on the selection of the attracting branch. When $X^0 \approx b$, each branch has a roughly equal probability of being selected, such that the variance for $t \to \infty$ becomes $\lesssim ((c-b)^2 + (a-b)^2)/2 = 100$. Due to this mixing effect of the noise, the closer X^0 to b and the larger δ, the higher the conditional variance.

The conditional variance $\Sigma^2_X(\boldsymbol{\xi})$ presented above can not allow one to estimate the variance in X due to the noise only, because of the information loss incurred with the conditional expectation. Indeed, $\mathbb{E}\{\mathbb{V}\{X \mid \boldsymbol{\xi}\}\} = V_{\mathrm{noise}} + V_{\mathrm{mix}}$, such that the averaging of Σ^2_X combines the pure noise and mixed contributions to the variance, without possibility of subsequently separating them. To compute the partial variances V_{noise} and V_{mix}, it is necessary to go through the Sobol decomposition of X as discussed in Section 4. The time evolutions of the partial variances of X are shown in Figure 17. The results indicates that the parametric uncertainty is responsible for most of the variance at any time t, as V_{par} dominates all other

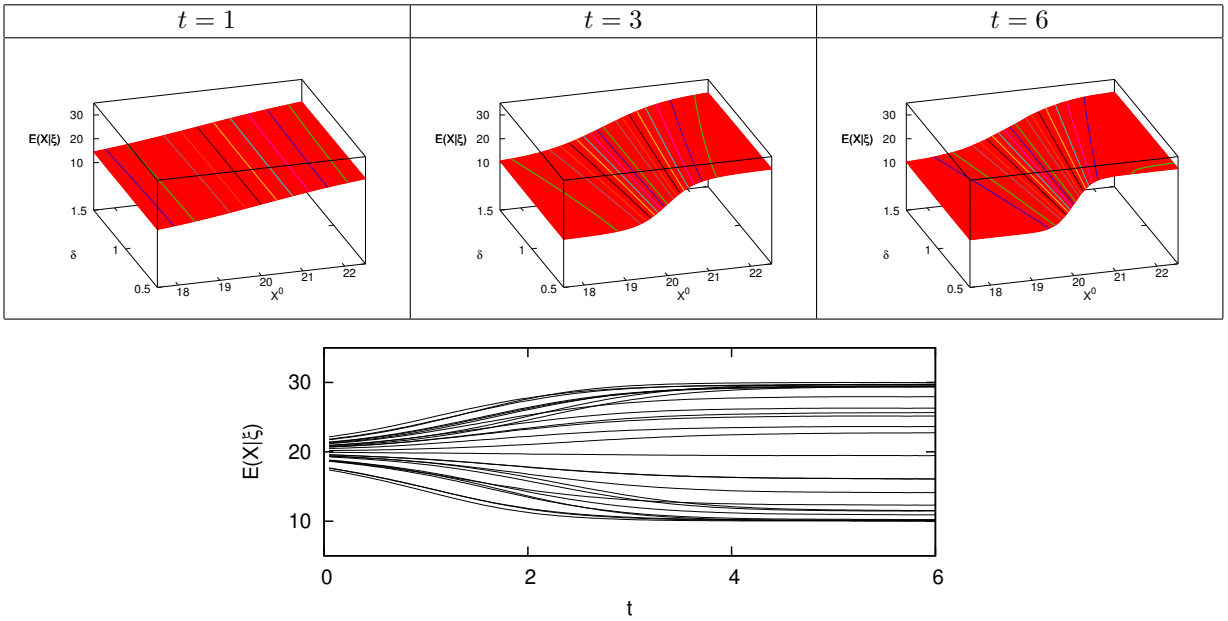

Figure 15: Conditional expectation $\mathbb{E}\{X \mid \boldsymbol{\xi}\}$. The top plots present the surface response of the conditional expectation as a function of $X^0(\xi_1)$ and $\delta(\xi_2)$ at selected times, as indicated. The bottom plot depicts trajectories of $\mathbb{E}\{X \mid \boldsymbol{\xi}\}$ for a sample set of $\boldsymbol{\xi}$. The computations use an adaptive MW discretization with $S_{\mathrm{Nr,No}}$, Nr = 6 and No = 2, and uncertain system parameters $X^0 \sim \mathcal{R}[17.5, 22.5]$ and $\delta \sim \mathcal{R}[0.5, 1.5]$.

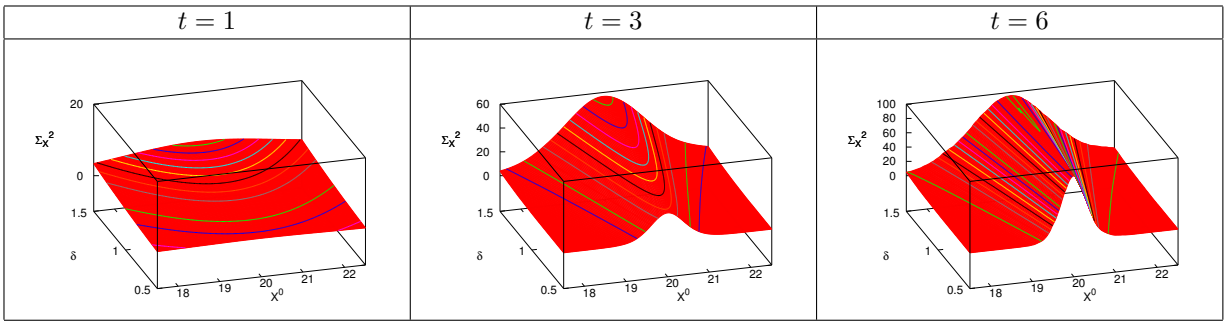

Figure 16: Conditional variance $\Sigma^2_X(\boldsymbol{\xi})$ at selected times, as indicated. The conditional variance is plotted as a function of the uncertain initial condition $X^0(\xi_1)$ and noise level $\delta(\xi_2)$. The computations use an adaptive MW discretization with $S_{\mathrm{Nr,No}}$, Nr = 6 and No = 2, and uncertain system parameters $X^0 \sim \mathcal{R}[17.5, 22.5]$ and $\delta \sim \mathcal{R}[0.5, 1.5]$.

partial variances. The pure noise contribution V_{noise} is seen to initially be larger than V_{mix}, but levels off at $t \approx 2.5$, while V_{mix} continues to increase, becomes larger than V_{noise} for $t \geq 3$ and barely achieves its asymptotic value for $t = 6$ (as for V_{par}). The differences in the response time scales between the curves of V_{par} and V_{mix} in the one hand, and V_{noise} on the other hand, can be explained as follows. The pure noise variance quickly saturates because the mixing effect of the noise on the branch selection occurs during the early transient only, while it essentially only induces fluctuations of the trajectory toward the selected branch later on (see Figure 11). On the contrary, the time scale of V_{par} and V_{mix} curves is related to the characteristic time of the noise-free system, which is governed by γ, and corresponds roughly to the average characteristic time of the deterministic system to reach the closest stable branch for the set of initial conditions.

To complete the analysis of the variance in the bifurcation system, we change the range of variation for the noise level from $[0.5, 1.5]$ to $[1.5, 2.5]$, still with a uniform distribution. Therefore, the range of δ has the same extent, but δ has now a expected value twice as large as previously. By increasing the average noise level, we expect an enhanced W mixing of the trajectories over a larger range of initial conditions. This can be verified in Figure 18, whose results should be compared with those of Figure 15; specifically, the surface

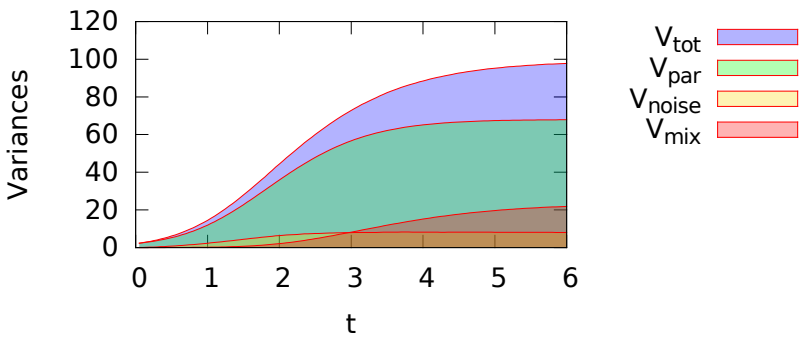

Figure 17: Partial variances of the stochastic process $X(t)$. The computations use an adaptive MW discretization with $S_{\mathrm{Nr,No}}$, $\mathrm{Nr} = 6$ and $\mathrm{No} = 2$, and uncertain system parameters $X^0 \sim \mathcal{R}[17.5, 22.5]$ and $\delta \sim \mathcal{R}[0.5, 1.5]$.

responses of the conditional expectation $\mathbb{E}\{X \mid \boldsymbol{\xi}\}$ (top plots) now exhibit less variability with respect to X^0. Also, the $\boldsymbol{\xi}$-sample set of trajectories for $\mathbb{E}\{X \mid \boldsymbol{\xi}\}$ (bottom plot) does not extend anymore over the whole range $[a, b]$ denoting that even for the extreme values of X^0 the noise induces a non vanishing probability of selecting the attracting branch farthest from the starting point X^0. In addition, the lower ξ-variability in $\mathbb{E}\{X \mid \boldsymbol{\xi}\}$ in Figure 18, compared to Figure 15, indicates a lower partial variance V_{par} as we will seen later.

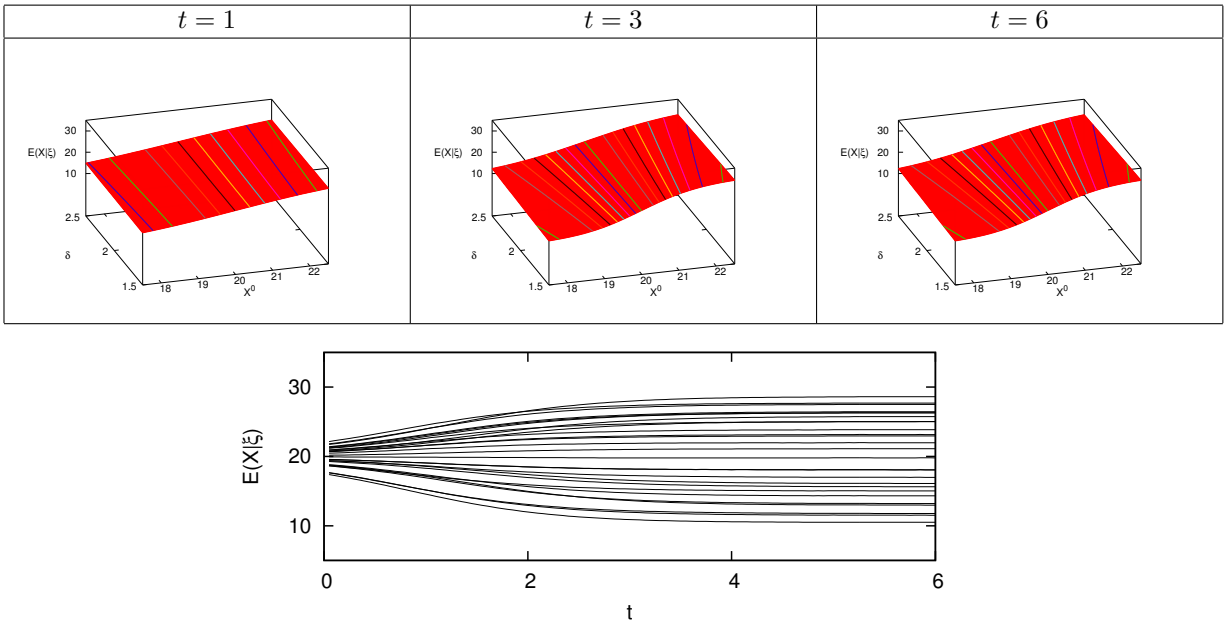

Figure 18: Conditional expectation $\mathbb{E}\{X \mid \boldsymbol{\xi}\}$. The top plots present the surface response of the conditional expectation as a function of $X^0(\xi_1)$ and $\delta(\xi_2)$ at selected times, as indicated. The bottom plot depicts trajectories of $\mathbb{E}\{X \mid \boldsymbol{\xi}\}$ for a sample set of $\boldsymbol{\xi}$. The computations use an adaptive MW discretization with $S_{\mathrm{Nr,No}}$, $\mathrm{Nr} = 6$ and $\mathrm{No} = 2$, and uncertain system parameters $X^0 \sim \mathcal{R}[17.5, 22.5]$ and $\delta \sim \mathcal{R}[1.5, 2.5]$.

Figure 19 presents the surface response of $\Sigma^2_X(\boldsymbol{\xi})$ for $t = 1, 3$ and 6. The structures of the surface responses are similar to the previous case with a lower average noise level (see Figure 16), but with a less marked peak for $X^0 \approx b$ for $t > 1$. In fact, $\Sigma^2_X(\boldsymbol{\xi})$ presents less variabilities with $\boldsymbol{\xi}$ than previously. Note also that the maxima in Σ^2_X are larger than previously observed for $t = 1$ and $t = 3$ (that is at intermediate time in the transient), while the maxima are essentially equal for the two cases at $t = 6$. Again, this trend is explained by the higher mixing during the transient stage for higher average noise level. On the contrary, when the system converges toward its asymptotic limit, and the dynamics reduce to fluctuations around the attracting branches, the magnitude of the stochastic fluctuations have a less significant impact on the

variance (also because the local distributions around each attracting branches are skewed toward the unstable point). Finally, comparison of the Σ_X^2 plots in Figures 16 and Figure 19 indicates that the *total* variance due to the noise is larger for the case with larger average δ, since its $\boldsymbol{\xi}$-averages are larger.

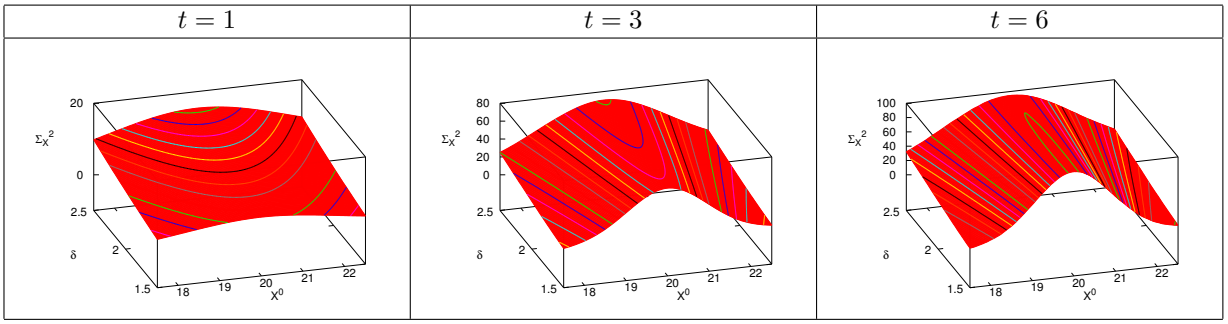

Figure 19: Conditional variance $\Sigma_X^2(\boldsymbol{\xi})$ at selected times, as indicated. The conditional variance is plotted as a function of the uncertain initial condition $X^0(\xi_1)$ and noise level $\delta(\xi_2)$. The computations use an adaptive MW discretization with $S_{\mathrm{Nr,No}}$, $\mathrm{Nr} = 6$ and $\mathrm{No} = 2$, and uncertain system parameters $X^0 \sim \mathcal{R}[17.5, 22.5]$ and $\delta \sim \mathcal{R}[1.5, 2.5]$.

At this point, it can be concluded that increasing the expected value of δ while keeping a constant variability range yields a lower partial variance V_{par} and a larger total variance due to the noise $\mathbb{E}\left\{\Sigma_X^2\right\} = V_{\mathrm{noise}} + V_{\mathrm{mix}}$. It remains to determine the effect of increasing $\mathbb{E}\{\delta\}$ on the overall variance $\mathbb{V}\{X\}$, and how it changes the partial variances V_{noise} and V_{mix}. For the first point, the left plot in Figure 20 compares the total variances and total contribution of the noise to the variance (sum of V_{noise} and V_{mix}) for the two expected values of δ. It shows that as previously stated, the total noise contribution increases significantly from the case $\mathbb{E}\{\delta\} = 1$ to $\mathbb{E}\{\delta\} = 2$. For the total variance however, it is seen that during the transient ($t < 3$) increasing $\mathbb{E}\{delta\}$ increases $\mathbb{V}\{X\}$ (labelled V_{tot} in the plot), though by a small fraction. On the contrary, when the system approaches its equilibrium ($t > 3$), the increase of $\mathbb{E}\{\delta\}$ results in a slightly lower total variance. Again, the small decay with increasing $\mathbb{E}\{\delta\}$ of the asymptotic total variance can be explained by the skewness (toward the unstable point) in the distributions of the fluctuations around the two attracting branches.

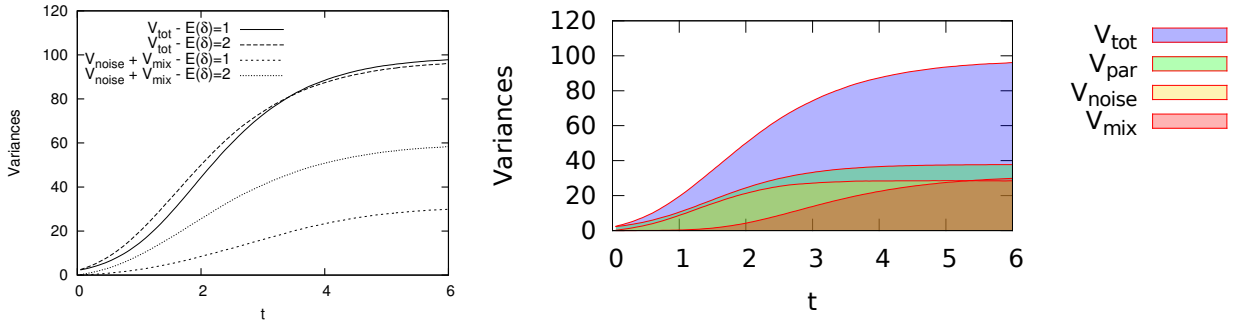

Figure 20: Left: comparison of the total variances $\mathbb{V}\{X\}$ and total noise contributions $V_{\mathrm{noise}} + V_{\mathrm{mix}}$ to the variance, for two expected values of $\mathbb{E}\{delta\} = 1$ and 2. Right: partial variances of the stochastic process $X(t)$ for the case $\mathbb{E}\{\delta\} = 2$. The computations use an adaptive MW discretization with $S_{\mathrm{Nr,No}}$, $\mathrm{Nr} = 6$ and $\mathrm{No} = 2$, and uncertain system parameters $X^0 \sim \mathcal{R}[17.5, 22.5]$, and $\delta \sim \mathcal{R}[0.5, 1.5]$ or $\delta \sim \mathcal{R}[1.5, 2.5]$.

The complete variance decomposition of X is presented in the right plot of Figure 20 for $\mathbb{E}\{\delta\} = 2$; and should be contrasted with the decomposition of the variance for $\mathbb{E}\{\delta\} = 1$ reported in Figure 17. The main differences in the partial variances concern first the important reduction of V_{par}, which however remains dominant with respect to V_{noise}. Second, both the noise and mixed contributions to the variance have significantly increased. However, contrary to the case with $\mathbb{E}\{\delta\} = 1$, it is seen that the asymptotic values for V_{noise} and V_{par} are now very close. It can then be concluded that increasing $\mathbb{E}\{\delta\}$, keeping its variability range constant, not only increases the part of variance incurred to the noise only, but also its interaction with the parameters.

7. Discussion and conclusions

This paper has developed a PC analysis of stochastic differential equations driven by additive or multiplicative Wiener noise. A Galerkin formalism was adopted, that naturally led to the definition of a hierarchy of stochastic differential equations governing the evolution of the PC modes. The resulting representation was exploited to perform an orthogonal decomposition of the process variance, and consequently identify contributions arising from the uncertainty in parameters, the stochastic forcing, and a coupled term. Additional insight into the contribution of individual sources of uncertainty was gained through a Sobol–Hoeffding decomposition of the PC representation itself. This naturally leads to the definition of sensitivity indices that quantify the contributions of Wiener noise and of different sources of parametric uncertainty to the total variance of the process.

Implementation of the present formalism was illustrated in light of two model problems. The first considers a linear system consisting of a scalar SODE with uncertain drift and diffusion coefficients. Simulations were conducted to illustrate the implementation of the Galerkin formalism, which relied on a Wiener–Legendre basis to represent the impact of parametric uncertainties. A variance analysis based on the resulting PC representations was conducted, which demonstrated the ability to decompose the variance into contributions from the Wiener noise and parameters alone as well as a mixed term that quantifies their interaction. The computations were also used to illustrate the ability to quantify sensitivities and consequently isolate the impact of different sources of uncertainty.

In addition, a non-linear problem was also considered that involves an unstable fixed point. To capture the discontinuity in a stochastic setting, the Galerkin methodology relied on a multiwavelet basis to represent the impact of parametric uncertainty. Computed results were used to demonstrate the capability of capturing and analyzing complex stochastic dynamics, namely in the present of stochastic forcing and parametric uncertainties leading to steep variations and bifurcation.

We finally remark that the variance decomposition performed in the present study hinged on the availability of a stochastic PCE. While we focused on applying a Galerkin methodology to construct such expansions, this task could generally be achieved through sampling methods that enable one to compute, separately, the solution moments with respect to the random parameters and the Wiener noise. A delicate aspect in the implementation of non-intrusive methodologies, however, concerns the robustness of the estimates in presence of Wiener noise. For instance, recent experiences [36] have shown that straightforward implementation of projection methods to evaluate moments with respect to uncertain parameters can be prone to large errors in the presence of noisy data, whereas Bayesian regression techniques [36, 37, 31, 32, 29, 30, 1] can effectively overcome these hurdles, provided likelihood functions can be defined that suitably capture the effects of the stochastic forcing.

The development of sampling-based methods and efficient algorithms that implement these methods would be particularly attractive in complex settings where the implementation of Galerkin or intrusive methodologies is not feasible. This would be the case when the model structure effectively precludes or renders impractical the computation of averages over the stochastic process. Relevant examples include molecular dynamics (MD) simulations or stochastic simulation algorithms (SSA). Whereas the generation of multiple realizations of the solution for a given value of uncertain parameters is conceptually straightforward, open questions still remain regarding how to investigate the dependence of the solution with respect to the uncertain parameters for a fixed realization of the noise, and whether it is possible to decompose the variance of the solution or of selected QoIs into contributions that isolate the impact of individual sources of uncertainty. We plan to address these questions in future work.

A. Time-integration methods for Stochastic ODEs

In this work, we make use of different time-integration methods to compute the evolutions of the vector $\boldsymbol{X}(t,\omega)$ of expansion coefficients arising from the parametric discretization of X. Two different ways can be taken for the derivation of time-integration schemes; the first one starts from the continuous problem for $\boldsymbol{X}$ in (13) and proceeds with its time-discretization; the second one considers instead as a starting point the

discrete time-scheme for the process X and proceeds with its stochastic Galerkin projection to derive the discretized governing equation for the coefficients vector.

The two approaches may not be completely equivalent, because of truncation errors, and we start with the second one.

Time-integration schemes for scalar ODEs. We shall detail the derivation of 3 integration methods in this paper, the Euler, Milstein and (one) secon-order Runge-Kutta methods. Consider the (autonomous) SODE,

$$dX = C(X)dt + D(X)dW, \quad X(t=0) = X^0.$$

The Euler method for solving this ODE can be expressed as

$$X^{i+1} = X^i + C(X^i)\Delta t + D(X^i)\Delta W^i, \tag{39}$$

where $\Delta t > 0$ is the time-step, X^i the approximate solution at time $t_i = i\Delta t$, and $\Delta W^i \doteq W(t_{i+1}) - W(t_i)$ are the Wiener increments. The Euler method yields an error $\mathcal{O}(\Delta t^{1/2})$.

The Milstein method [26] involves an additional term accounting for the dependence of the drift coefficient on X; it is expressed as

$$X^{i+1} = X^i + C(X^i)\Delta t + D(X^i)\Delta W^i + \frac{1}{2}D(X^i)D_x(X^i)((\Delta W^i)^2 - \Delta t), \tag{40}$$

and has an error $\mathcal{O}(\Delta t)$. Here, we have denoted $D_x(X)$ the derivative of $D(X)$ with respect to X. It is clear that the Milstein and Euler methods are the same in the case of additive noise ($D_x = 0$).

Finally, we shall also consider one second-order *Runge–Kutta method* [39],

$$X^{i+1} = X^i + \left[C(X^i) + C(\tilde{X}^{i+1})\right]\frac{\Delta t}{2} + \left[D(X^i) + D(\tilde{X}^{i+1})\right]\frac{\Delta W^i}{2} - \frac{1}{2}D(X^i)D_x(X^i)\Delta t. \tag{41}$$

This is a two-stage method where the provisional value $\tilde{X}^{i+1}$ corresponds to the one-step Euler method applied to X^i, namely $\tilde{X}^{i+1} = X^i C(X^i)\Delta t + D(X^i)\Delta W^i$. It has an error $\mathcal{O}(\Delta t^2)$ for essentially twice the cost of the previous methods.

Galerkin projection of the time-integration schemes. Following the notation of Section 3 consider the expansion $X = \sum_{k=0}^{P} [X_k]\,\Psi_k$ and $\boldsymbol{X} \in \mathbb{R}^{P+1}$ the vector of expansion coefficients.

The stochastic Galerkin projection of the *Euler scheme* in (39) gives

$$[X_k]^{i+1} = [X_k]^i + [C_k]\,(\boldsymbol{X}^i)\Delta t + [D_k]\,(\boldsymbol{X}^i)\Delta W^i, \quad k = 0, \cdots, P \tag{42}$$

where

$$[C_k]\,(\boldsymbol{X}) \doteq \left\langle C\left(\sum_{l=0}^{P}[X_l]\,\Psi_l\right), \Psi_k\right\rangle, \quad \text{and} \quad [D_k]\,(\boldsymbol{X}) \doteq \left\langle D\left(\sum_{l=0}^{P}[X_l]\,\Psi_l\right), \Psi_k\right\rangle,$$

are the projection coefficients of the drift term and diffusion coefficient.

For the *Milstein scheme* in (40), we obtain

$$[X_k]^{i+1} = [X_k]^i + [C_k]\,(\boldsymbol{X}^i)\Delta t + [D_k]\,(\boldsymbol{X}^i)\Delta W^i + \frac{1}{2}\,[M_k]\,(\boldsymbol{X}^i)((\Delta W^i)^2 - \Delta t), \tag{43}$$

where

$$[M_k]\,(\boldsymbol{X}) \doteq \left\langle D\left(\sum_{l=0}^{P}[X_l]\,\Psi_l\right) D_x\left(\sum_{l=0}^{P}[X_l]\,\Psi_l\right), \Psi_k\right\rangle.$$

Finally, the Galerkin projection of the second-order *Runge–Kutta scheme* in (41) leads to

$$[X_k]^{i+1} = [X_k]^i + \left[[C_k]\,(\boldsymbol{X}^i) + [C_k]\,(\tilde{\boldsymbol{X}}^{i+1})\right]\frac{\Delta t}{2} + \left[D_k(\boldsymbol{X}^i) + D_k(\tilde{\boldsymbol{X}}^{i+1})\right]\frac{\Delta W^i}{2} - \frac{1}{2}\,[M_k]\,(\boldsymbol{X}^i)\Delta t, \tag{44}$$

where $\tilde{\boldsymbol{X}}^{i+1}$ is the provisional coefficients vector solution of (42).

Remarks. The projection of the three integration schemes above requires the evaluation of projections of $C(\boldsymbol{X})$, $D(\boldsymbol{X})$ and possibly $D(\boldsymbol{X})D_x(\boldsymbol{X})$ onto the stochastic basis. This may be an issue in case of highly non-linear C and D. In the present work, where the drift term and diffusion coefficient considered are all polynomials in X, these projections raise no major difficulties [9], except eventually for a significant computational complexity in the case of large projection basis. Presently, for polynomials C and D with degree > 1 in X, we rely on pseudo-spectral projection to maintain a reasonable computational complexity. The pseudo-spectral projection of polynomial non-linearities rely on the Galerkin interpretation of each individual multiplication [23, 9]. These approximate projections yield truncation errors that must be monitored to ensure they do not compromise the overall accuracy of the computation.

The development of the numerical time-integration schemes above was based on the Galerkin projection of the discrete (in time) schemes. The time-discretization of the continuous equation for the vector $\boldsymbol{X}$ is an alternative as we mentioned previously. For the Euler method, the two alternatives coincide. However, for the Milstein and RK-2 methods, the two approaches may not exactly result in the same schemes, depending on the choice of the method used for the projection of the non-linearities and inherent truncation errors. In addition, if one considers applications of the Milstein or RK-2 methods to the whole system of ODEs, the computation of the Jacobian of the vector of modes $\boldsymbol{D}$ is required. This Jacobian matrix will be large for large expansion bases, but could eventually be computationally more effective than the projection of the product $D(\boldsymbol{X})D_x(\boldsymbol{X})$ in the integration schemes above. This point would require further analyses and numerical experiments to investigate the respective merits of the alternatives.

References

[1] Alexanderian, A., Rizzi, F., Rathinam, M., Le Maître, O., Knio, O., 2014. Preconditioned Bayesian Regression for Stochastic Chemical Kinetics. Journal of Scientific Computing 58, 592–626.

[2] Alpert, B., 1993. A class of bases in L_2 for the sparse representation of integral operators. SIAM J. Math. Anal. 24, 246–262.

[3] Bell, J., Garcia, A., Williams, S., 2010. Computational fluctuating fluid dynamics. ESAIM: Mathematical Modelling and Numerical Analysis 44, 1085–1105.

[4] Buizza, R., Miller, M., Palmer, T. N., 1999. Stochastic representation of model uncertainties in the ECMWF ensemble prediction system. Quart. J. Roy. Meteor. Soc. 125, 2887–2908.

[5] Cameron, R., Martin, W., 1947. The orthogonal development of nonlinear functionals in series of Fourier-Hermite functionals. Annals of Mathematics 48, 385–392.

[6] Chen, J.-B., Ghanem, R., Li, J., 2009. Partition of the probability-assigned space in probability density evolution analysis of nonlinear stochastic structures. Probabilistic Engineering Mechanics 24, 27–42.

[7] Choi, M., Sapsis, T., Karniadakis, G., 2013. A convergence study for SPDEs using combined Polynomial Chaos and Dynamically-Orthogonal schemes. Journal of Computational Physics 245, 281–301.

[8] Crestaux, T., Le Maître, O., Martinez, J., 2009. Polynomial chaos expansion for sensitivity analysis. Reliability Engineering & System Safety 94 (7), 1161–1172.

[9] Debusschere, B., Najm, H., Pébay, P., Knio, O., Ghanem, R., Le Maître, O., 2004. Numerical challenges in the use of polynomial chaos representations for stochastic processes. SIAM J. Sci. Comp. 26 (2), 698–719.

[10] Donev, A., Garcia, A. L., de la Fuente, A., Bell, J. B., 2011. Diffusive transport by thermal velocity fluctuations. Phys. Rev. Lett. 106, 204501.

[11] E, W., Liu, D., Vanden-Eijnden, E., 2007. Nested stochastic simulation algorithms for chemical kinetic systems with multiple time scales. Journal of Computational Physics 221 (1), 158 – 180.

[12] Ghanem, R., Spanos, P., 1991. Stochastic Finite Elements: A Spectral Approach. Springer Verlag, New York.

[13] Giles, M., 2008. Multi-level Monte Carlo path simulation. Operations Research 56 (3), 607–617.

[14] Gillespie, D., 1976. A general method for numerically simulating the stochastic time evolution of coupled chemical reactions. Journal of Computational Physics 22 (4), 403 – 434.

[15] Gillespie, D., 1977. Exact stochastic simulation of coupled chemical reactions. The Journal of Physical Chemistry 81 (25), 2340–2361.

[16] Gillespie, D., 1992. A rigorous derivation of the chemical master equation. Physica A: Statistical Mechanics and its Applications 188 (13), 404 – 425.

[17] Gillespie, D., 2001. Approximate accelerated stochastic simulation of chemically reacting systems. The Journal of Chemical Physics 115 (4), 1716–1733.

[18] Gillespie, D., Petzold, L., 2003. Improved leap-size selection for accelerated stochastic simulation. The Journal of Chemical Physics 119 (16), 8229–8234.

[19] Hoel, H., von Schwerin, E., Szepessy, A., Tempone, R., 2014. Implementation and analysis of an adaptive multilevel Monte Carlo algorithm. Monte Carlo Methods and Applications 20 (1), 1–41.

[20] Khouider, B., Biello, J., Majda, A., 2010. A stochastic multicloud model for tropical convection. Comm. Math. Sci. 8, 187–216.

[21] Landau, L., Lifshitz, E., 1959. Fluid Mechanics. Pergamon.

[22] Le Maître, O., Ghanem, R., Knio, O., Najm, H., 2004. Uncertainty propagation using Wiener-Haar expansions. J. Comput. Phys. 197 (1), 28–57.

[23] Le Maître, O., Knio, O., 2010. Spectral Methods for Uncertainty Quantification. Springer, New York, NY.

[24] Le Maître, O., Najm, H., Ghanem, R., Knio, O., 2004. Multi-resolution analysis of Wiener-type uncertainty propagation schemes. J. Comput. Phys. 197, 502–531.

[25] Le Maître, O., Najm, H., Pébay, P., Ghanem, R., Knio, O., 2007. Multi-resolution-analysis scheme for uncertainty quantification in chemical systems. SIAM J. Sci. Comput. 29 (2), 864–889.

[26] Mill'shtejn, G. N., 1975. Approximate integration of stochastic differential equations. Theory Probab. Appl. 19 (3), 557–562.

[27] Porta Mana, P., Zanna, L., 2014. Toward a stochastic parameterization of ocean mesoscale eddies. Ocean Modelling 79, 1–20.

[28] Rathinam, M., Petzold, L., Cao, Y., Gillespie, D., 2003. Stiffness in stochastic chemically reacting systems: The implicit tau-leaping method. The Journal of Chemical Physics 119 (24), 12784–12794.

[29] Rizzi, F., Jones, R., Debusschere, B., Knio, O., 2013. Uncertainty quantification in MD simulations of concentration driven ionic flow through a silica nanopore. Part I: sensitivity to physical parameters of the pore. J. Chem. Phys. 138, 194104.

[30] Rizzi, F., Jones, R., Debusschere, B., Knio, O., 2013. Uncertainty quantification in MD simulations of concentration driven ionic flow through a silica nanopore. Part II: uncertain potential parameters. J. Chem. Phys. 138, 194105.

[31] Rizzi, F., Najm, H., Debusschere, B., Sargsyan, K., Salloum, M., Adalsteinsson, H., Knio., O., 2012. Uncertainty quantification in MD simulations. Part I: Forward propagation. Multiscale Model. Simul. 10, 14281459.

[32] Rizzi, F., Najm, H., Debusschere, B., Sargsyan, K., Salloum, M., Adalsteinsson, H., Knio., O., 2012. Uncertainty quantification in MD simulations. Part II: Bayesian inference of force-field parameters. Multiscale Model. Simul. 10, 14601492.

[33] Sapsis, T., Lermusiaux, P., 2012. Dynamical criteria for the evolution of the stochastic dimensionality in flows with uncertainty. Physica D 241, 60–76.

[34] Sapsis, T., Majda, A., 2013. Blended reduced subspace algorithms for uncertainty quantification of quadratic systems with a stable mean state. Physica D 258, 61–76.

[35] Sapsis, T., Majda, A., 2013. Statistically accurate low-order models for uncertainty quantification in turbulent dynamical systems. Proceedings of the National Academy of Sciences 110 (34), 13705–10.

[36] Sargsyan, K., Debusschere, B., Najm, H., Marzouk, Y., 2009. Bayesian inference of spectral expansions for predictability assessment in stochastic reaction networks. Journal of Computational and Theoretical Nanoscience 6 (10), 2283–2297.

[37] Sargsyan, K., Safta, C., Debusschere, B., Najm, H., 2012. Multiparameter spectral representation of noise-induced competence in bacillus subtilis. IEEE/ACM Transactions on Computational Biology and Bioinformatics.

[38] Sobol, I. M., 1993. Sensitivity estimates for nonlinear mathematical models. Math. Modeling and Comput. Exper. 1, 407–414.

[39] Tocino, A., Ardanuy, R., 2002. Runge-Kutta methods for numerical solution of stochastic differential equations. J. Comp. App. Math 138 (2), 219–241.

[40] Tryoen, J., Le Maître, O., Ern, A., 2012. Adaptive anisotropic spectral stochastic methods for uncertain scalar conservation laws. SIAM J. Sci. Comp. 34 (5), 2459–2481.

[41] Wiener, N., 1938. The homogeneous chaos. Am. J. Math. 60, 897–936.

[42] Zarate, J. D., J.V.Sengers, 2006. Hydrodynamic fluctuations in fluids and fluid mixtures. Elsevier Science Ltd.